Recent Progress and Development of Self-Aligned Focusing Schlieren

Wayne E. Page*, Matthew T. Boyda†, Timothy W. Fahringer‡, Joshua M. Weisberger§, and Brett F. Bathel¶
NASA Langley Research Center, Hampton, VA, 23681

Mark P. Wernet‖
NASA Glenn Research Center, Cleveland, OH 44135

James T. Heineck**
NASA Ames Research Center, Moffett Field, CA 94035

A broad range of developments and applications of self-aligned focusing schlieren (SAFS) systems is presented. The replacement of the Ronchi ruling (RR) with a μLCD was demonstrated with digital SAFS, which provides the ability to modulate the pattern and orientation without physical intervention. Additionally, replacement of the traditional RR with spectral-spatial filters was demonstrated to yield the ability to simultaneously image horizontal and vertical index of refraction gradients using two separate wavelengths. The application of the Scheimpflug principle to SAFS systems enables off-axis imaging and allowed for extended fields-of-view to be captured using a two-camera system. The addition of a plenoptic camera to a baseline SAFS system enables refocusing capabilities, which is demonstrated on two jets offset along the optical axis. Furthermore, application of an event-based camera to SAFS was shown to enable acquisition of sparse, spatio-temporal data. Beyond the listed developments, SAFS was applied to difficult and constraining facilities, such as the National Full-Scale Aerodynamics Complex (NFAC) 80- by 120-ft Wind Tunnel and the Thermal Acoustic Engines (TAE) rig at NASA Ames Research Center and NASA Glenn Research Center, respectively. Behavior of Ronchi rulings, Rochon prisms, and the use of quarter-wave plates versus quarter-wave films are evaluated to provide insight for future experimental design of SAFS-systems.

I. Introduction

The origins of schlieren as a flow visualization technique dates as far back as the 17th century [1]. Since then, increased understanding and numerous developments have led to the broad adoption and use of schlieren-based techniques for flow visualization. All schlieren-based techniques are utilized to image gradients of the refractive index in transparent media, which when utilized for gases (or liquids) is related to the density gradients via the Gladstone-Dale relation [2]. Therefore, schlieren is commonly used in flows with density gradients, such as compressible, reacting, or high-temperature flows.

A wide variety of schlieren techniques have been developed, ranging from traditional Toepler's lens/mirror-type schlieren [3], background-oriented schlieren (BOS) [4–7], focusing schlieren [8–11], among other specialized techniques. All of these techniques provide measurements or images that constitute, to some degree, a path-integrated measurement of the refractive index gradients throughout the measurement volume. Since the majority of measurement volumes can be far larger than the relevant scales for the flow of interest, as they extend between lenses or mirrors for Toepler-like setups and from camera to background for BOS setups, much of the signal captured in images using these schlieren methods is not pertinent to the flow features of interest within the measurement volumes. The result can be images that are contaminated with flow features or other artifacts (e.g., window scratches, window imperfections, or room thermal

*Pathways Graduate Student, Advanced Measurements and Data Systems Branch, AIAA Student Member.
†Pathways Graduate Student, Advanced Measurements and Data Systems Branch, AIAA Student Member.
‡Research Engineer, Advanced Measurements and Data Systems Branch.
§Research Engineer, Advanced Measurements and Data Systems Branch, AIAA Senior Member.
¶Research Engineer, Advanced Measurements and Data Systems Branch, AIAA Associate Fellow.
‖Senior Research Engineer, Optics and Photonics Branch, AIAA Associate Fellow.
**Photographic Technologist, Experimental Aero-physics Branch, AIAA Associate Fellow.

gradients) outside the domain of interest. The focusing schlieren technique, however, only provides in-focus imagery of gradients within a narrow depth-of-focus while maintaining sensitivity similar to conventional schlieren.

Focusing schlieren setups, such as that shown schematically in Fig. 1a, differ somewhat from that of conventional schlieren setups. On one side of the measurement volume, a source grid consisting of an arrangement of alternating opaque and clear parallel lines is projected through the measurement volume to act as a set of extended schlieren light sources. Subsequently, the projection is imaged through a field lens and focused onto a cutoff grid. The cutoff grid is a scaled version of the source grid and acts in a similar manner to the knife edge in conventional schlieren. On the other side of the cutoff grid, a camera can be placed to image the resulting schliere produced from the focusing schlieren setup. This results in a measurement volume that is constrained along the optical axis by the depth-of-focus of the optical setup and constructive signals of the overlapping regions of the multiple extended light sources from the source grid.

For conventional focusing schlieren significant care is taken to align the projected source grid onto the cutoff grid, ensuring the projected size of the source grid matches the size of the cutoff grid, the lines from both grids are parallel, and there exists a small offset between the two grids. The precise alignment required can prove to be time-consuming and problematic when utilizing the technique under various experimental conditions that may cause the alignment to drift (e.g. wind tunnel vibrations, thermal expansion, etc.). Various efforts have been explored to improve the usability of focusing schlieren [12–15]. Yet, most of these implementations still prove to be time-consuming when ensuring the precise alignment between the source and cutoff grids.

Recently, a technique referred to as self-aligned focusing schlieren (SAFS) has been developed that mitigates the need for individuals to align the source and cutoff grids [16, 17]. The self-aligning nature of SAFS is a result of the use of a single source grid that is projected through the system and re-imaged back on to itself, which can be achieved with retro-reflective material or a mirror-like surface. For the source grid to also act as its cutoff grid, a polarizing prism (such as a Rochon or Wollaston prism) is utilized to refract the light of the re-imaged grid projection with proper manipulation of the polarization state of light passing through the system. The inherent self-aligned nature of the system eliminates the need for alignment of separate grid elements, which enables both the ability to achieve signal within minutes of installation and easy adjustment if experimental conditions change. Furthermore, the sensitivity of the system is robust against vibration and small impacts to the system.

In spite of the major improvements SAFS provides compared to conventional focusing schlieren, there are still a variety of characteristics that can limit its usefulness. For instance, SAFS based experiments require the use of a source grids that are typically manufactured with patterned lines of chrome deposited on a glass substrate with a singular spatial frequency, typically given in line pairs per mm (lp/mm), commonly referred to as Ronchi rulings, although other source grid patterns can be used. SAFS experiments usually require a variety of source grids to help optimize the sensitivity given a specific experimental setup, or to provide the ability to adapt the experimental setup throughout a test campaign (e.g., change the focal plane, field lens, etc.). The variety of spatial frequencies required and the limitation of having single frequency physical patterned Ronchi rulings can increase setup time and cost and limit flexibility. Facilities with restrictive physical access can also prove to be limiting when utilizing SAFS. Firstly, limited physical access can make it cumbersome or time-consuming to adjust focal planes or switch out or rotate Ronchi rulings, which is required to optimize the sensitivity of a SAFS systems and target different density gradient directions, respectively. Secondly, facilities or experiments may have restrictive viewing access that would necessitate an off-axis viewing angle, which can be problematic for SAFS depending on the plane of interest and the plane that the retro-reflective material needs to be applied too. Furthermore, SAFS images can require significant bandwidth and memory for storage, particularly for high-speed or lengthy acquisitions, even though the schliere within an image may only subtend parts of the frame.

The current work details recent research and development at NASA to address these limitations of SAFS. Various adaptations of SAFS have been developed at NASA Langley Research Center to address the above constraints and to improve the overall usability of SAFS-based techniques. Digital self-aligned focusing schlieren [18] (D-SAFS) was developed to mitigate constraints related to both the physical access to the source grid and the need for a variety of manufactured source grids. D-SAFS accomplishes this by utilizing a digital transparent micro liquid crystal display (μLCD) in combination with a linear polarizer to act as the source grid. D-SAFS enables the ability to rapidly and remotely change the source/cutoff grid pattern. This includes changing the spatial frequency, changing the orientation, or switching to less conventional patterns. Another alternative to achieve flexibility in imaging multiple gradients exists with the creation and use of spectral-spatial filters where both the horizontal and vertical gradients can be measured simultaneously. Another adaptation utilized Scheimpflug adjustments to the internal optical components to enable off-axis viewing [19]. The off-axis viewing enables the image plane to be rotated in such a way that it is not orthogonal to the optical axis, and may be aligned to observe features that would only be partially resolved otherwise. This allows for focused schlieren imaging to be performed in ground test facilities with limited optical access, but also enables the

use of SAFS with other diagnostics that typically compete for optical access. The addition of a plenoptic camera utilized within a SAFS system can enable translation and selection of the focusing plane post experiment. Finally, event-based cameras [20] can be utilized to provide sparse, high-speed, spatio-temporal data streams that may be capable of enabling advanced data processing techniques or insight beyond the capabilities of traditional frame-based systems.

Beyond the limitations addressed with these adaptations, the current manuscript details a couple of recent applications of SAFS to difficult or constrained facilities, such as imaging at a large-scale facility or through curved windows. Furthermore, component trade studies are performed to illustrate both the behavior and importance of various components utilized within a SAFS systems. These trade studies are limited to the spatial resolution and sensitivity effects from various Ronchi rulings, polarization and sensitivity effects from various Rochon prisms, and the comparison of the use of quarter-wave plates and quarter-wave films for SAFS-based systems.

II. SAFS System Overview

A. Baseline System

A schematic of both a baseline SAFS system is shown in Fig. 1b, and is used here to describe the system's operation, with the polarization state of the outgoing and incoming light shown in the legend at the right. This is the same baseline configuration that has been used in previous works [16, 17], and while many configuration changes can be made, they will be addressed in Section II.B and in the subsequent sections of this paper. A light source emits light toward a polarizing beamsplitter (PBS), oriented to reflect linear vertically polarizer (LVP) light onto the main optical axis of the system. A condenser-diffuser (CD) and a linear polarizer (LP^1) are added between the light source and the PBS to loosely collimate, diffuser, and polarize the light. The light that is subsequently reflected through the PBS passes through a Ronchi ruling (RR), and the field lens (FL) projects an image of the RR onto the retroreflective background (RBG) on the opposite side of the density object of interest, acting as a source grid. The LVP light that passes through the polarizing Rochon prism (RP) remains unrefracted, and is converted to right circularly polarized (RCP) light after passage through the quarter-wave plate (QWP).

When the RCP light is incident on the RBG, the handedness is reversed, and the incoming light is now left circularly

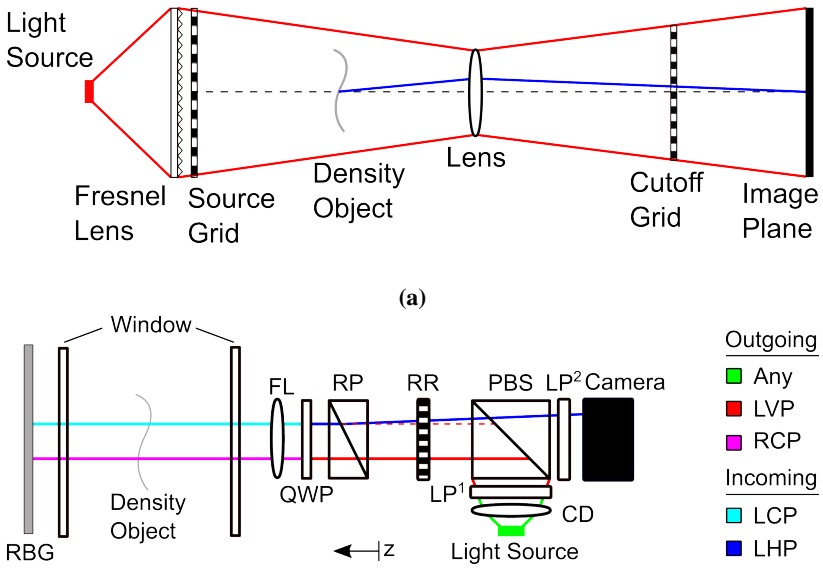

Fig. 1 Schematic of a conventional focusing schlieren system (top), and a schematic of the baseline SAFS system, with light polarization state identified in the legend for the outgoing and incoming directions of light propagation (bottom).

polarized (LCP), which after passage through the QWP in the opposite direction is converted to linear horizontally polarized (LHP) light. This LHP light is slightly refracted by the RP, and the re-imaged grid on the RR is slightly offset in the plane of the RR, orthogonal to the direction of the grid lines, providing the knife-edge cutoff akin to a conventional schlieren image. The LHP light transmits through the PBS and a second linear polarizer (LP^2) oriented such that only LHP light transmits through, and was imaged on a camera sensor through a relay lens.

B. Other SAFS System Configurations

A variety of simple adaptations to a baseline SAFS system can be made without significant changes to overall performance. The placement of the RP prior to the FL can be limiting on the achievable focus or sensitivity. Conversely, the RP can be moved aft of the FL to allow the fields to move closer to both the RR and camera. Albeit, the QWP needs to be moved with the RP to achieve the required polarization rotation. In doing so, the QWP can be placed directly after the RP, or can be moved to the opposite side to be near or incident on the RBG. In this instance, care needs to be taken to ensure that all of the light projected through the system passes through the QWP, which can be difficult or cost-prohibitive due to the size of the projection. In these cases, the QWP can be replaced with a quarter-wave film (QWF) that can be directly placed on to the RBG.

Similar to other schlieren-based techniques, various light sources such as white-light LEDs, monochromatic LEDs, or lasers can be used for illumination. Although, the use of LEDs require relatively long pulse-widths to provide sufficient illumination that may result in motion blur in the acquired images. Pulsed laser illumination can be used in place of the LED, although care should be taken to avoid laser speckle, which can be mitigated by utilizing a laser source with low-coherence. Furthermore, typical SAFS systems utilize a diffuser to provide a uniform intensity profile, which can be achieved in a variety of fashions. Commonly used options are the condenser-diffuser lens and an engineered diffuser, such as a circle pattern engineered diffuser [21] or holographic diffuser. The condenser-diffuser lens can provide a loose collimation of the diffuse light enhancing the light collection efficiency, but may not provide a perfectly uniform illumination profile. Conversely, the use of a circle pattern or holographic diffuser can create a fairly uniform diffuse light profile from a Gaussian source. A lens (e.g., plano-convex, Fresnel, etc.) can be used in conjunction with the diffuser to improve the light collection efficiency. If the light profile still exhibits high intensity near the center of the field-of-view an apodizing filter may be used to enhance illumination uniformity.

C. Basic Image Processing

In many instances, SAFS images do not require further image processing to clearly identify the flow features of interest. However, there are some image enhancement methods that can be used, depending on the imaging scenario, outlined in more detail in Refs. [21, 22]. The simplest method of enhancing weaker flow structures and to achieve a uniform background intensity over the entire field-of-view is to use either background-subtraction or background-division. Flowcharts of these methods, used in scenarios where either flow-off reference images are available or where they are not, are included in Section II of Ref. [22]. In some instances, when the focus plane is close to the RBG, a faint image of the Ronchi ruling lines are visible in the SAFS images, due to the narrow, but finite depth-of-focus of the camera and relay lens. In these instances, an FFT filtering of the images works well, where a 2D FFT is first computed from the image, the two peaks from the Ronchi ruling grid frequency are removed from the FFT image, and the inverse FFT is computed, resulting in a spatially filtered image with the influence of the Ronchi ruling grid lines removed (see the flowchart in Fig. 2 of Ref. [22]). When using finer Ronchi rulings (lower linepair spacing), the influence of diffraction on the final images can be distracting, and so a point spread function (PSF) filtering can be computed to reduce the higher order diffraction images as discussed in Ref. [18]. If the frame rate of the SAFS images is sufficiently high, a spectral proper orthogonal decomposition (SPOD) can be performed to obtain the spatial and spectral content of the flow structures in the image sequence, as shown in Ref. [21]. Note that this list is not exhaustive, only providing references to those techniques used with existing SAFS data, and that any number of image processing methods not included here can be used to enhance the data product.

III. Digital SAFS (D-SAFS)

A digital self-aligned focusing schlieren system adapts a traditional SAFS system by replacing the physical grid element with a digital transparent micro liquid crystal display (μLCD). The transparent μLCD is comprised of a matrix

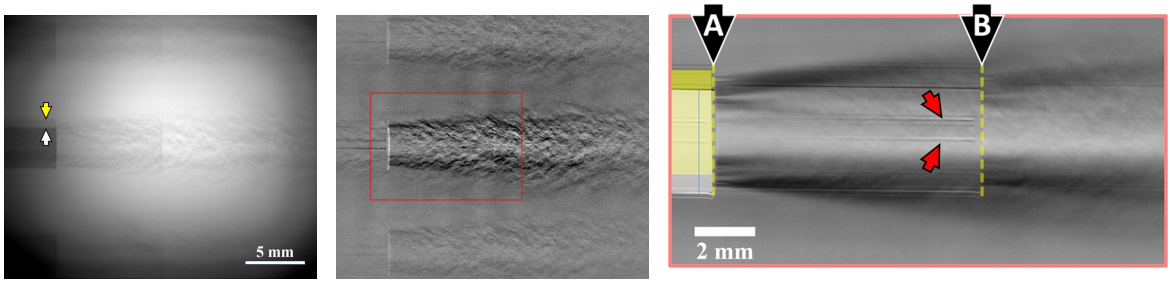

(a) (b) (c)

Fig. 2 From left to right (a) instantaneous raw, (b) instantaneous background-subtracted, and (c) time-averaged background-subtracted D-SAFS images of a difluoroethane jet issuing into air with a grid frequency of approximately 4 lp/mm.

of liquid crystal pixel elements. Each liquid crystal element is controlled by an applied electric field that rotates the orientation of the organic molecules within the element, which effectively acts as a polarization modulator. Therefore, the polarization state can be controlled spatially. Consequently, a binary pattern, such as a Ronchi ruling, can be displayed on the μLCD that generate regions of distinct and discrete polarization states. Ideal operation of a μLCD would have regions where the initial linear polarization state is unaffected and regions where the initial linear polarization state is rotated by 90°. This pattern, in combination with the rejection of linear vertically polarized light from both the polarizing beamsplitter and linear polarizer, effectively acts as the physical grid element in a conventional SAFS system. Therefore, the binary pattern can be varied by changing the displayed pattern, which can be done in a rapid and remote manner. Further details about the implementation and operation about D-SAFS can be found in Bathel *et al.* [18].

An initial experiment was performed with a difluroethane jet (compressed gas duster) issuing into a quiescent air environment through a 2.7 mm inner diameter needle providing a turbulent flow with varying density gradient scales, which was imaged with the D-SAFS system described in Bathel *et al.* [18]. Figure 2 shows an example instantaneous raw, instantaneous background-subtracted, and time-averaged background-subtracted image, respectively. The images presented in Fig. 2 exhibit a number of behaviors that restrict the quality of the images. First, the background illumination appears to mask out the underlying schlieren signal, which is likely due to strong reflections off the μLCD. The quality can be enhanced via background subtraction of a flow-off image, but other issues become apparent as in Fig. 2b. Primarily, the presence of repeated image artifacts can be noted in both Figs. 2b and 2c as a result of significant diffraction of light through the pixels in the μLCD. This is particularly evident in Fig. 2c where the signal starting at plane A is repeated downstream at plane B.

Characterization of the polarization retarder effects of a μLCD (Epson L3C07U-85G13) was performed to inform future D-SAFS experimental design. Five different low-power lasers (Thorlabs PL255, CPS450, PL201, PL202, and CPS670F) were utilized with different wavelengths (404.7 nm, 447.9 nm, 516.5 nm, 638.9 nm, and 675.3 nm) to provide monochromatic, polarized light. The input polarization state was varied between horizontal, vertical, and 45° linearly polarized light using a Glan-Thompson (GTP) calcite polarizer (Thorlabs GTH10M-A). Subsequently, the light is passed through the μLCD and an aperture (AP) before being measured via a polarimeter (Thorlabs PAX1000VIS) as shown in Fig. 3. Both sides of the μLCD were probed as light has to pass through the incident and opposing sides (as defined by the manufacturer) of a μLCD for the operation of a D-SAFS system. The displayed gray level was varied from 0 to 255 in increments of 8 to control the output polarization state of the μLCD.

The polarimeter allows for both the azimuth and ellipticity to be measured as a function of time as all of the parameters are varied. The polarimeter was set to a basic sample rate of 200 Hz with two full spins of the quarter-wave plate and a 2048-point FFT for measurement of the polarization state. These settings limited the measurement to a sampling rate of 50 Hz. For each measurement state, 128 data points were taken to allow for the computation of the mean and variance of the measurement.

The resulting measurements of azimuth and ellipticity are shown in Fig. 4 for an input state of LHP on the incident side of the μLCD. The measurements exhibit a significant wavelength dependence for both the behavior of the azimuth and ellipticity as a function of displayed gray level. The azimuth is always rotated nearly 90°, but the gray level that this occurs at is shifted based on input wavelength. This behavior is also observed in the minimum achieved ellipticity, as

this "valley" is shifted to the left as the wavelength is decreased. Yet, after the peak occurs the ellipticity shows an increase until it plateaus at some value, after which no control is shown by varying the grey level. The noted plateaus show the most significant wavelength dependence. For an ideal D-SAFS system, the μLCD needs to be able to achieve both a 90° rotation in azimuth and a 0° ellipticity. For the wavelengths shown, it is apparent from Fig. 4b that this is only possible for the 404 nm and 447 nm light source as they both have a zero crossing in the ellipticity with an accompanying non-zero rotation in polarization azimuth..

Experimental work was performed using a helium jet issuing from a 2.7 mm inner diameter needle into a quiescent environment to determine the qualitative effect that a binary pattern displayed with different gray levels would have on the captured schlieren images. A pulsed LED light source centered near 613 nm was used to provide illumination. The μLCD was set to display two different RR patterns of alternating lines. One pattern was set to alternate between 0 and 255 to maximize the rotation in azimuth and minimize the ellipticity at 635 nm. The other pattern was set to alternate between 0 and 155, which corresponds to the approximate "valley" shown in Fig. 4b. A comparison of two instantaneous background-subtracted images from the two patterns is shown in Figure 5. Both images still suffer from the occurrence repeated artifacts from the diffraction, but the image taken with the 0 to 255 pattern shows increased contrast when compared to the one taken with a grid pattern of 0 to 150.

An attempt was also made to obtain images with LED light centered near 450 nm, which should be capable of providing a 90° rotation with zero ellipticity. Yet, the image quality was significantly affected by back reflections into the camera. To isolate the issue, transmission measurements, presented in Fig. 6, were performed on the RP. For these transmission measurements, the output power six low-power lasers of varying wavelength (Thorlabs PL255, CPS450, PL201, PL202, CPS670F, and PL205) was obtained and compared to measurements of the transmitted power through a quartz/glass RP with a splitting angle of 7.5 arcmin from the same manufacturer. Results show that there is a significant reduction in transmission when operated at lower wavelengths for the RP used in the D-SAFS systems (United Crystals, G/Q-15 arcmin), but the G/Q-7.5 arcmin RP shows a small reduction in transmission and should be more ideal for future experiments.

IV. Scheimpflug SAFS Imaging

A baseline SAFS system is configured with both the background plane and density object plane, $\mathcal{P}_{BG}$ and $\mathcal{P}_{DO}$ respectively, oriented perpendicular to the optical axis. Yet, there exists a variety of experimental configurations or environments where the baseline configuration can be difficult to achieve due to this constraint. This necessitates configuration variations, such as application of RBG to non-planar surfaces or off-axis viewing that may require $\mathcal{P}_{BG}$ and/or $\mathcal{P}_{DO}$ to be oriented such that it is not normal to the optical axis. To achieve this with SAFS, adjustments can be made by the application of the Scheimpflug principle [23], which in traditional camera systems enables in-focus imaging at along planes that are not orthogonal to the optical axis. Bathel *et al.* [19] characterized the Scheimpflug imaging configuration of SAFS for a variety of applications in optically constrained environments.

One of the major advantages, and the focus within this manuscript, is that the application of the Scheimpflug principle enables adjacent SAFS systems to capture larger, temporally correlated fields-of-view. This is particularly useful with high-speed SAFS due to the reduction in field-of-view as the framing rate is increased, which is typical in the operation of high-speed camera systems. Figure 7 demonstrates the extended field-of-view configuration comprised of two high-speed SAFS systems with both at non-normal incidence to $\mathcal{P}_{BG}$ and $\mathcal{P}_{DO}$. This system demonstrates the

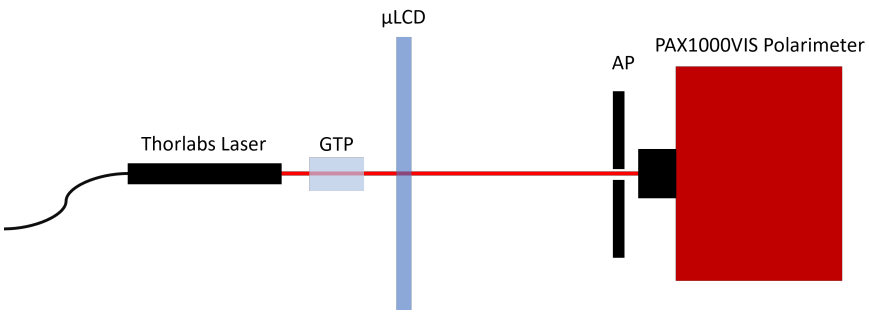

Fig. 3 Experimental setup for characterization of the μLCD effect on the polarization state.

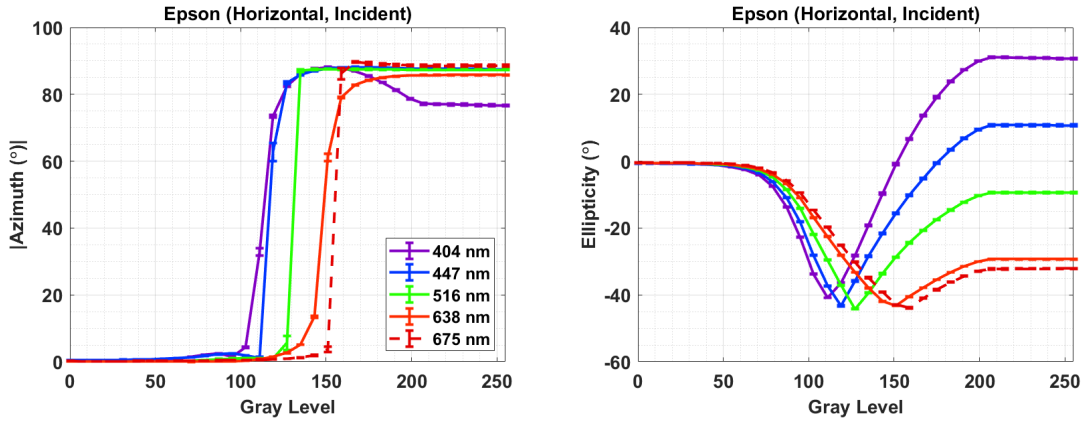

(a) (b)

Fig. 4 Measured absolute value of the azimuth (a) and ellipticity (b) as gray level is varied on the Epson μLCD with LHP on the incident side for various wavelengths.

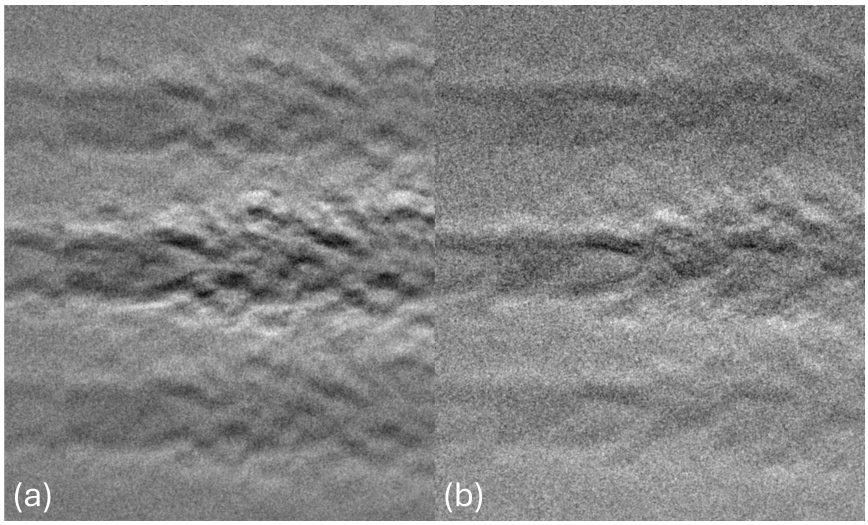

Fig. 5 Instantaneous background-subtracted D-SAFS images resulting to a binary grid pattern ranging from 0 **to** 255 **(a) and** 0 **to** 155 **(b)**

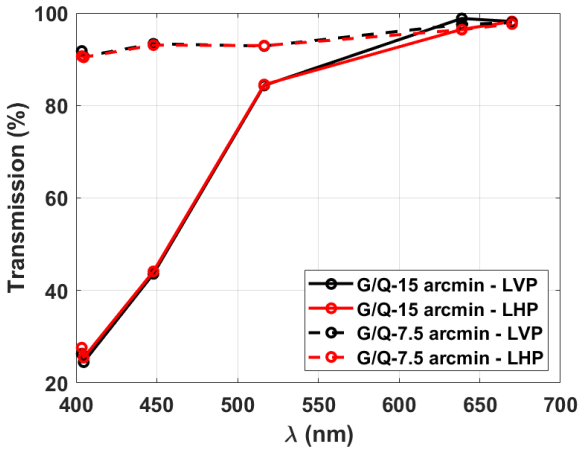

Fig. 6 Transmission of two different Rochon prisms with an input polarization of LVP (black) and LHP (red).

application of the Scheimpflug principle when both the RR plane, $\mathcal{P}_{RR}$, and the image sensor plane, $\mathcal{P}_{IM}$, must be angled. This requirement is a result of the off-normal imaging angles, α_i shown in Fig. 7, relative to the respective planes of incidences on which they are imaging or projecting.

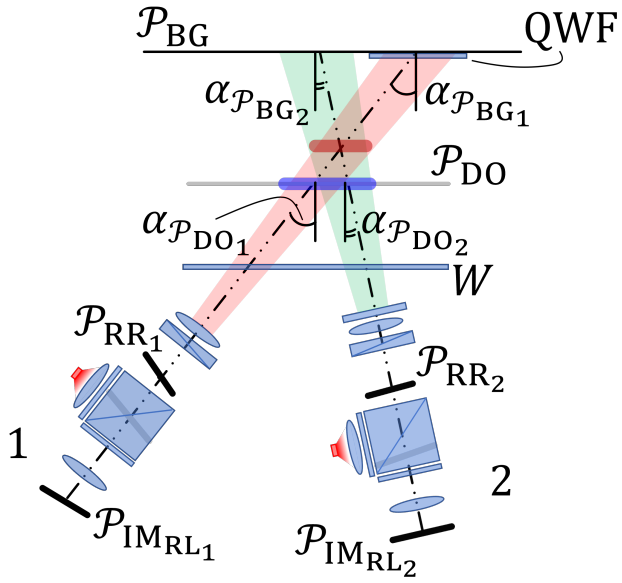

Fig. 7 Schematic of the extended field-of-view imaging configuration with two high-speed SAFS system, from Ref. [19].

Figure 8 shows several single-shot focused schlieren images separated sequentially in time by 5 ms that were taken from a larger sequence of images acquired at 100 kHz using the two-system configuration. The overlapping fields-of-view from each system are denoted above the top left image from the sequence. In these images, a jet of initially laminar compressed duster gas propagates from left to right. As the jet flow develops, the front of the jet begins to break down at t = 10 ms and shear layer instability waves begin to develop behind this leading edge at t = 15 ms. As the jet flow continues to develop, the presence of the shear layer instability waves advance rapidly upstream and eventually the jet begins to breakdown to turbulence, as observed at t = 25 ms. While in general, this two-system SAFS configuration is able to extend the field-of-view in any direction, this current application demonstrates a horizontal extension by stitching the two separate fields-of-view together while providing a nearly continuous intensity field between the two

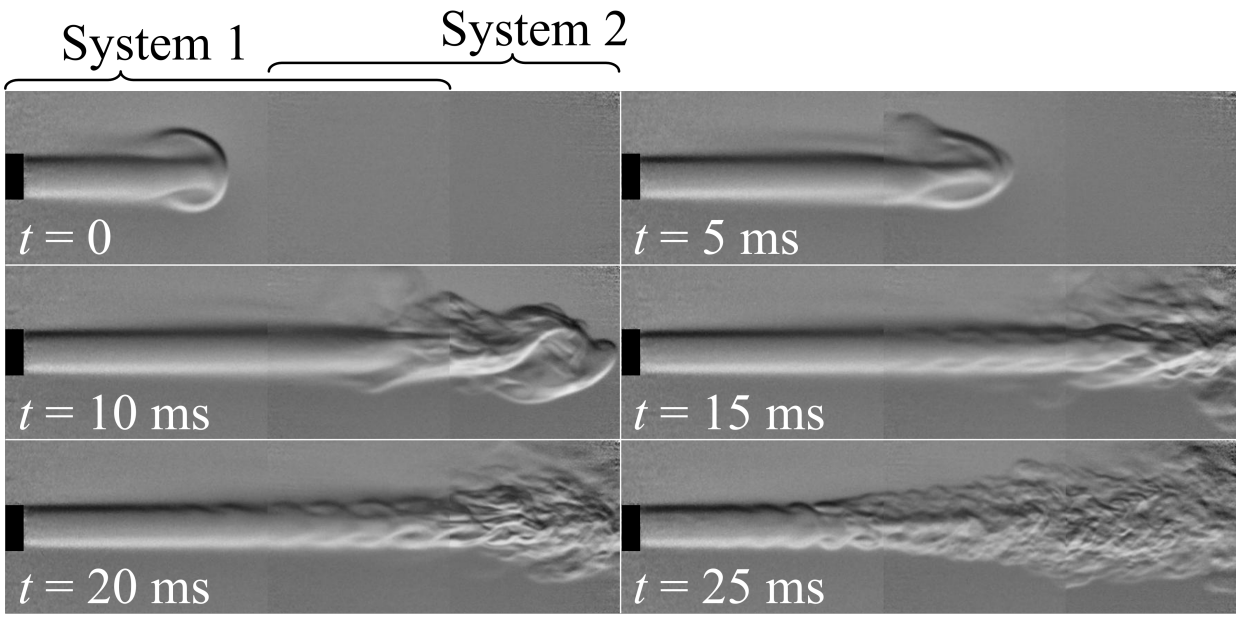

Fig. 8 High-speed focused schlieren image sequence acquired at 100 kHz (subsampled in 5 ms increments) with the field-of-view of two separate, synchronized SAFS systems stitched together to created an extended field-of-view showing the propagation of a jet of compressed duster gas.

systems with the final extended focused schlieren images having relatively good contrast and signal.

V. Plenoptic SAFS Imaging

While focusing schlieren systems can isolate flow features to a region with narrow depth-of-focus, using a conventional camera means that only one plane is imaged at every instant in time. By translating the camera along the optical axis, the plane of focus can be shifted from the farthest plane (at the retroreflective background) to the closest plane (near the field lens). This translation takes time, and images from each plane captured during camera translation are not time-correlated. This is not an issue that can be solved by higher frame rate cameras, since it is the camera translation (or the relay lens focus adjustment) that is the limiting factor. However, for relatively steady flows, this method of camera translation has been used with success. For example, the span-wise flow over an airfoil was able to be resolved at the NASA Langley Research Center's 0.3-M Transonic Cryogenic Tunnel (TCT) (see Figs. 8a and 8b in Ref. [22]).

A plenoptic camera, which includes a microlens array between the lens and image sensor, can be used to provide continuous refocusing of a flow field from a single acquired image [24]. Thus, the images at different focus planes can be acquired at the same instant in time, and an instantaneous 3D flowfield may be reconstructed. Plenoptic cameras have been used extensively for background-oriented schlieren (BOS) measurements [25, 26], and have found limited use in conventional focusing schlieren systems [27].

An example of the plenoptic camera used with a SAFS system is shown in Fig. 9. Here, two helium jets with an inner diameter of 4 mm are placed along the optical axis, with the upward-facing jet located at a nominal position of 0 mm and the downward-facing jet at −75 mm relative to the center focus plane. In both images, the flow from only the in-focus jet is clearly visible, with the out-of-focus jet structure being blurred. These images show the ability of the refocused images to "see through" the out-of-focus jet structures. Further results of the plenoptic SAFS imaging will be published in an upcoming article.

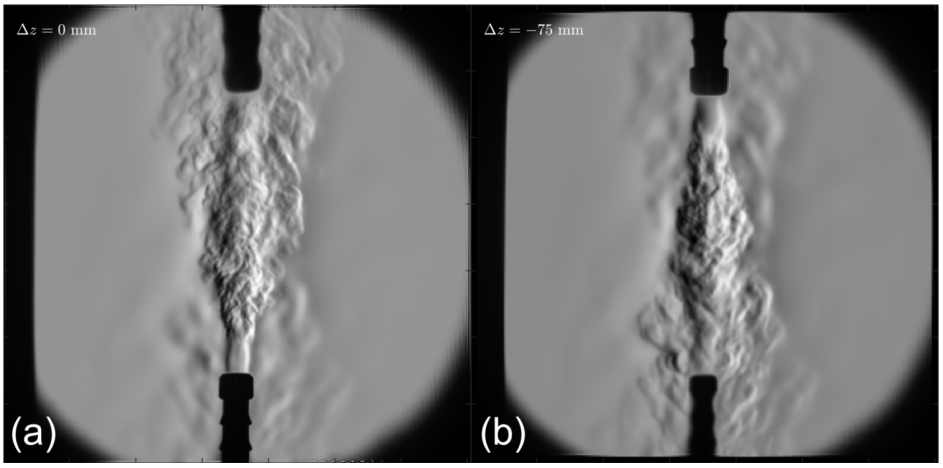

Fig. 9 Refocused plenoptic images of two opposed helium jets placed along the optical axis of the SAFS system, with the image focused at (a) the upward-facing jet at 0 mm and at (b) the downward-facing jet at 75 mm.

VI. Large-Scale Imaging

While typical implementations of the SAFS system are used in small/medium scale facilities, the system is not limited to use in only these smaller test sections, and has been successfully demonstrated in the largest wind tunnel facility in the world, the National Full-Scale Aerodynamics Complex (NFAC) 80- by 120-Foot Wind Tunnel at NASA Ames Research Center. In this test, shadowgraph and SAFS imaging were acquired of an 11-foot diameter rotor disk in order to image the vortex structure in hover.

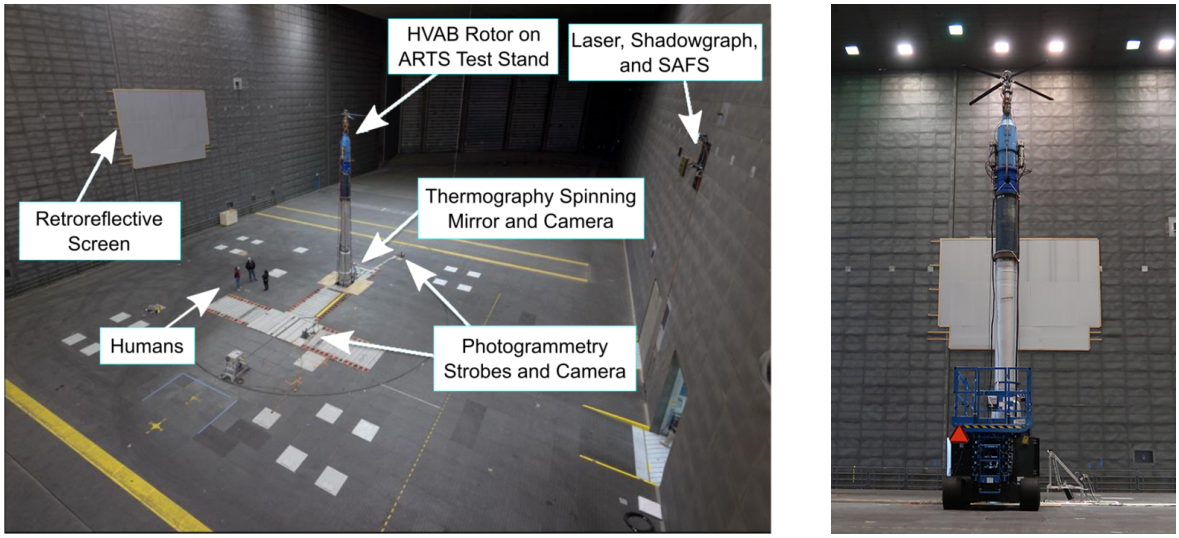

(a) **(b)**

Fig. 10 Images of the NFAC 80- by 120-Foot Wind Tunnel showing (a) the SAFS/shadowgraph systems on the right wall and retroreflective screen on the left wall, and (b) the rotor and retroreflective screen as imaged from the ground beneath the SAFS/shadowgraph systems.

An image of the NFAC can be seen in Fig. 10a, with the hover validation and acoustic baseline (HVAB) rotor installed on the test stand, the SAFS/shadowgraph systems located on the wall at the right, and the retroreflective screen on the wall at the left. Both the SAFS/shadowgraph systems and the retroreflective screens were located halfway up the

wall since the rotor was placed at the middle of the tunnel. Setup and alignment of the system was performed using a scissor jack to make adjustments to the SAFS system. Another view of the rotor and retroreflective screen can be seen in the image of Fig. 10b, taken from the ground beneath the SAFS system.

The retroreflective background for this installation had to encompass the full rotor disk and no less than 1.5 diameters of wake dimension. Thus, the background had to measure 28×20 feet (8.5×6 m). To accomplish this area twenty 4×8 foot panels of 0.25-inch-thick Gatorboard were laminated with two applications of 24-inch-wide Scotchlite 900x retroreflective tape from 50 yard rolls. A laminator was employed to make this an efficient and bubble-free operation. The mounting on the tunnel wall was accomplished by attaching furring strips of 1×3 inch wood with a 45° rip-cut to the perforated wall panels, such that each 4×8 board would be supported by two attachment lines. Matching furring strips were then placed in the crook of the 45° where each panel was glued and nailed to secure the panel to the mating furring strips. This method allowed for easy removal while assuring the best edge-to-edge mating of the panels.

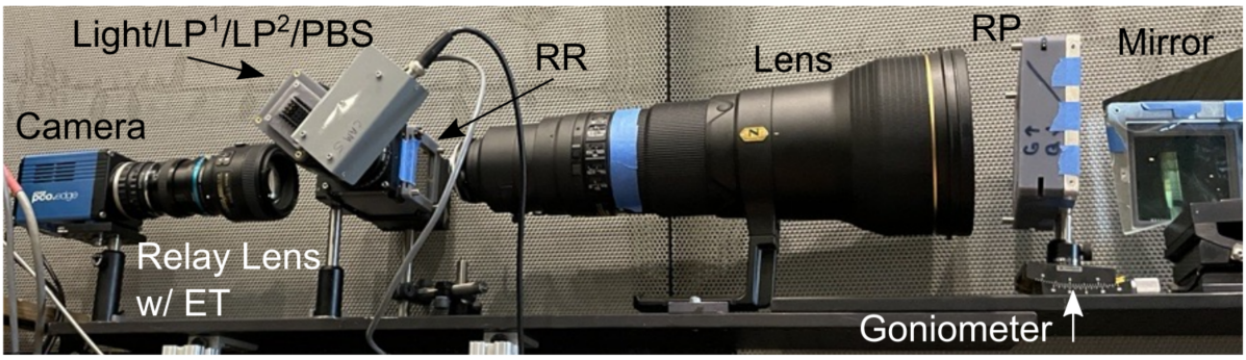

Fig. 11 Image of the SAFS system used at the NFAC 80- by 120-Foot Wind Tunnel at NASA Ames Research Center, mounted approximately 40 feet vertically on the wall, with the main optical axis aligned with the wall.

An image of the SAFS system installed at the NFAC is shown in Fig. 11. To avoid the SAFS system protruding out into the wind tunnel, the main optical axis of the system was aligned parallel to the wall, and a turning mirror used to reflect the optical axis across the tunnel toward the retroreflective screen. An LED illumination source is shown in this picture for the initial setup and alignment, but was switched to a laser illumination source for the test campaign. A 50 mm lens was attached to a PCO.edge camera via an adjustable extension tube. A 600 mm focal length field lens was used to project an image of the horizontally-oriented Ronchi ruling across the 120-foot width of the test section, while simultaneously providing the required field-of-view of the rotor blades at the tunnel centerline. The glass/quartz (7.5 arcmin) Rochon prism was mounted on a goniometer to provide sensitivity adjustment, since translation of the prism was limited (see Section X.D).

The full field-of-view shadowgraph image of the rotor is shown in Fig. 12a, where the edges of the retroreflective screen can be seen near the edges of the image. This shadowgraph image is able to view the entire rotor disk and a substantial region below the rotor, which was important for the vortex contraction measurements discussed in Refs. [28, 29]. A smaller field-of-view was chosen for the SAFS system, indicated with the dashed white rectangle in Fig. 12a, and a selected frame is shown in Fig. 12b. A cropped view of the shadowgraph image is shown in Fig. 12c for comparison, although note that the azimuth of the rotor blade and the field-of-view vary slightly between Fig. 12b and Fig. 12c. In the shadowgraph image, the vortices are clearly identified, and appear as predominantly black (or low intensity) structures due to their strong refractive nature and the large distance from the flow to the imaging screen. Only the primary vortex from each blade is visible. In the SAFS image, the primary vortex is again clearly visible, but now the bright/dark regions highlight the shape of the vortex more accurately. A secondary weaker vortex can also be seen faintly, which is absent in the shadowgraph images. The combination of the SAFS imaging system for high sensitivity but smaller field-of-view, and the shadowgraph system for lower sensitivity but larger field-of-view can provide a good balance between the two extremes for tests with differing scales and flow structure strengths.

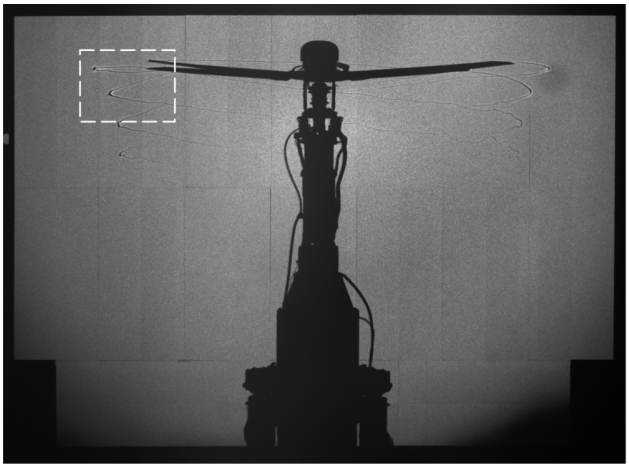

(a)

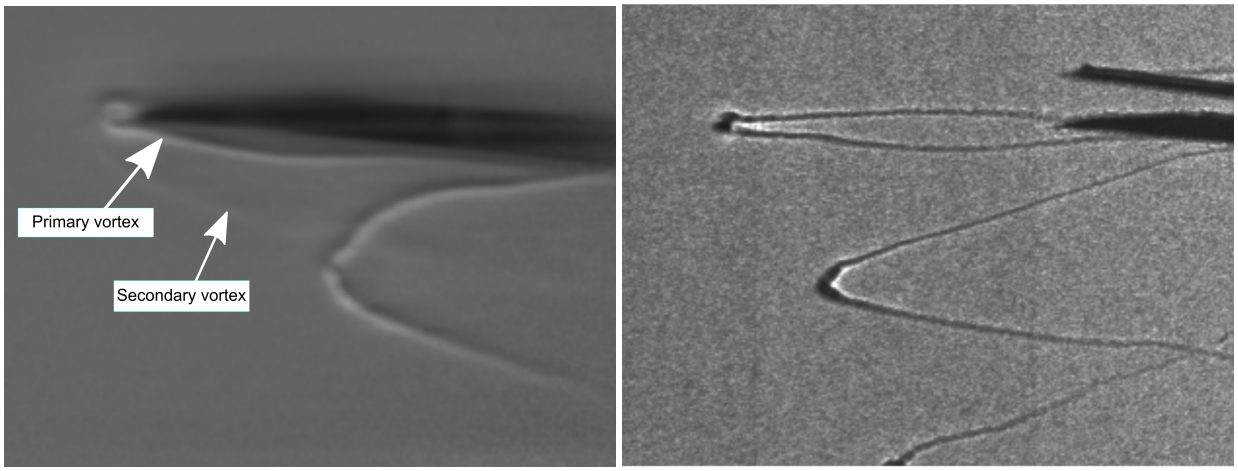

(b) (c)

Fig. 12 (a) Full field-of-view shadowgraph image of rotor disk, (b) full field-of-view SAFS image of the left side of the rotor disk, and (c) cropped shadowgraph field-of-view from (a) for comparison with SAFS image.

VII. Imaging through Curved Windows

Thermal Acoustic Engines (TAE) provide a means for efficiently transporting heat over long distances. In a recent investigation, a SAFS system was used to study the convective flow velocities inside of a TAE Rig at NASA Glenn Research Center. The objective of the work is to understand the relative phasing of the velocity fields inside TAEs versus the pressure fields. SAFS data were collected using a Photron high speed camera combined with a Cavilux pulsed laser system operating at 6 kHz and 30 ns pulse widths. The TAE uses a mechanically driven piston to generate acoustic waves (at 60 Hz) inside of a 50 mm inner diameter (ID) tube to a regenerator to provide heating and/or cooling [30]. Optical access for the SAFS system was obtained by fabricating an optical spool piece to fit into the TAE, which uses Helium as the working fluid at 450 psig. In order to withstand the pressure differential of 450 psi, a nominally 32 mm-thick window was required. Making the inside surface of the window curved to match the 50 mm tubing ID would result in a strong lensing effect. Instead, a fused quartz glass tube with 50 mm ID and 1 mm thick walls was used to match the inside ID of the TAE tubing, as shown in the CAD schematic of Fig. 13a and in the image of the setup of Fig. 13b.

A 32-mm-thick plane window was designed into the housing with an air gap between the outside of the glass tube and the inside surface of the plane window. The airspace between the outside of the 1-mm-thick cylindrical tube and

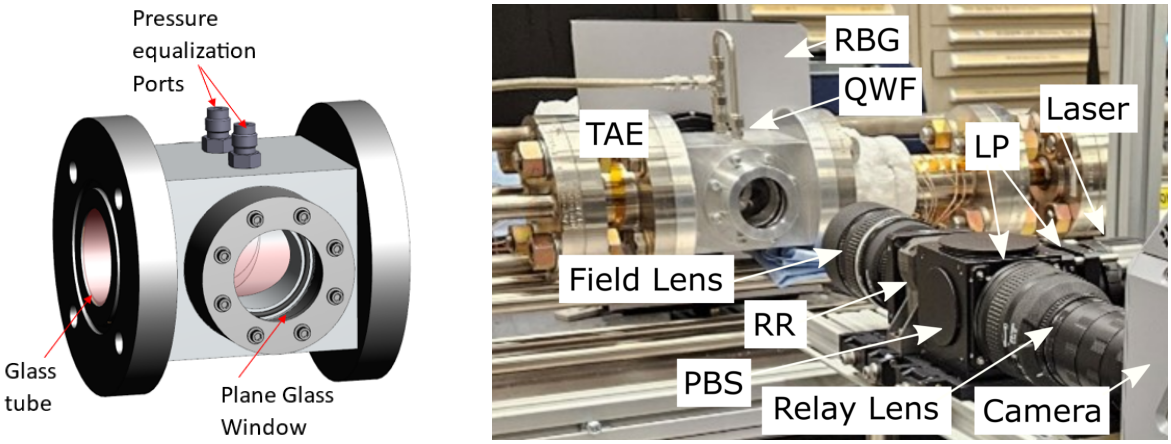

(a) **(b)**

Fig. 13 (a) Optical spool piece used to provide optical access into the TAE. The ports on top of the chamber are used to equalize the pressure between the inside of the glass tube and the air space between the plane glass window. (b) SAFS system looking through the optical spool piece installed into the TAE.

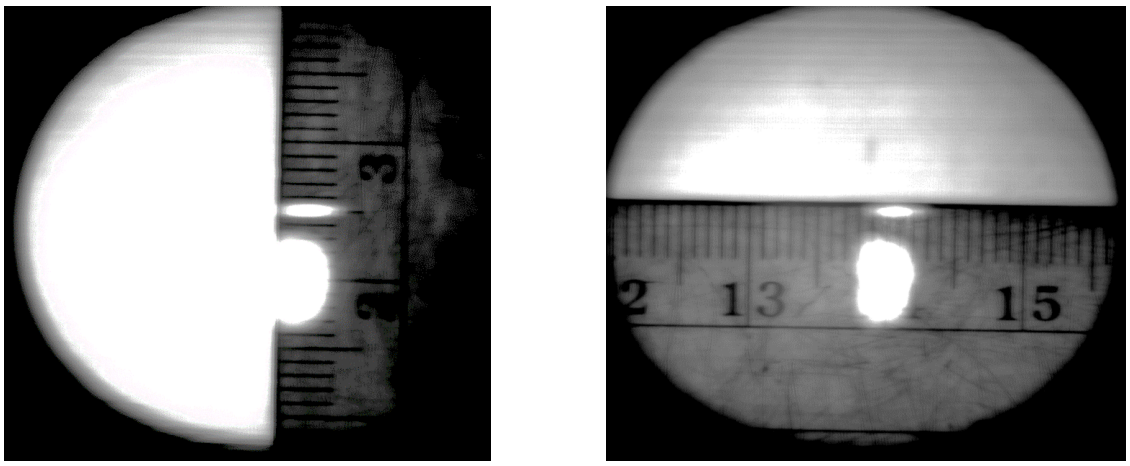

(a) **(b)**

Fig. 14 Images of a ruler at the center of the glass cylinder in the TAE spool piece, imaged by the SAFS camera, showing no distortion in the ruler in either direction.

the inside of the plane window was plumbed to be in equilibrium with the Helium gas within the TAE. Hence, the 1-mm-thick glass cylinder yielded minimal refractions while the 32-mm-thick plane parallel window withstands the large pressure differential without imparting additional refractions.

The cylindrical tube in the optical spool piece produces a lensing effect in the plane perpendicular to the axis of the tube. Orienting the SAFS Ronchi ruling grid lines parallel to the axis of the glass tube distorts the spacing between the projected grid lines on the retro-reflective background, which degrades the SAFS system performance. While a curved retro-reflective background could be used to mitigate this effect, the Ronchi ruling was instead oriented with the rulings perpendicular to the axis of the glass tube and the resulting refraction merely stretched the projected grid lines in the vertical direction, which did not affect the performance of the SAFS system. In fact, there was no significant optical distortion observed in the acquired SAFS images from within the optical spool piece. The diverging light cone from the SAFS system passes through the TAE optical spool piece and is distorted in the direction perpendicular to the axis of the tube. The light cone hits the retroreflective background, which now serves as the light source for the SAFS receiver.

The reflected light then passes back through the TAE optical spool piece which effectively negates the distortion that was imparted to the outgoing projected grid pattern. Figures 14a and 14b show the image of a ruler inserted vertically and horizontally inside the glass tube inside the TAE optical spool piece, respectively. Both images show no effective distortion of the ruler when imaged through the SAFS system.

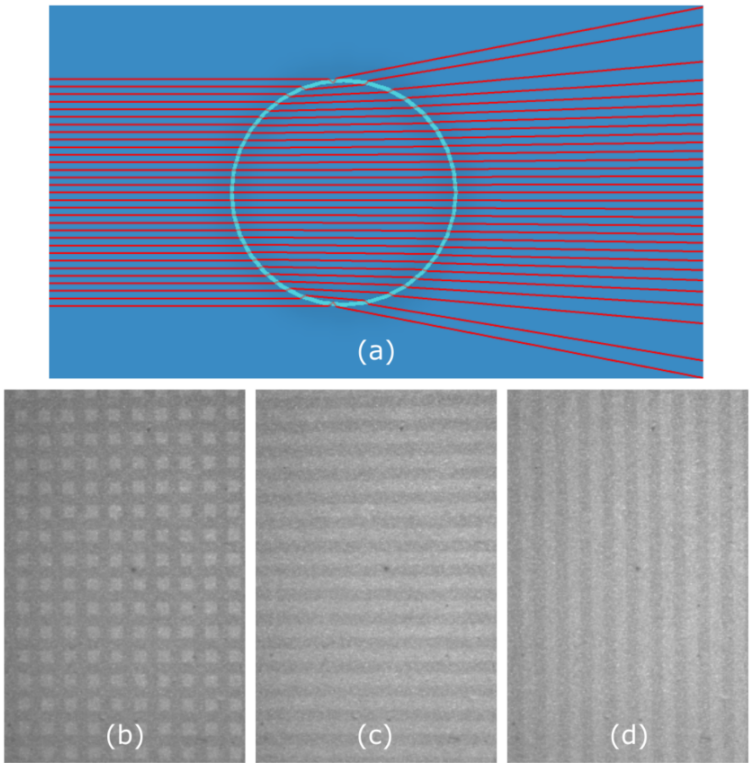

Fig. 15 (a) Representative ray trace through a glass cylinder illustrating the refraction causing a loss of some clear aperture through the cylinder. Images of (b) a projected 2D grid pattern without a cylindrical lens, (c) with a vertically-oriented cylindrical lens, and (d) with a horizontally-oriented cylindrical lens.

A ray-tracing simulation of the light passing through the glass cylinder is shown in Fig. 15(a), with collimated light entering the tube from the left, and the refracted rays exiting to the right, and the axis of the cylindrical glass tube is into the page. Note that the light entering the tube in the actual SAFS system is not necessarily collimated. As mentioned earlier, the glass tube acts as a weak cylindrical lens, and so will act to stretch the pattern in the direction orthogonal to the tube's axis. Example images of the projected grid pattern through a cylindrical lens are shown in Figs. 15(a,b,c). A 2D Ronchi ruling with a line spacing of 2 lp/mm in both directions is used, and the image of the projection of this grid on the background is shown in Fig. 15(b), without the inclusion of a cylindrical lens. Next, a weak cylindrical lens was placed after the field lens, first with its axis vertical and next with its axis horizontal, with the associated projected grid patterns shown in Figs. 15(c) and 15(d), respectively. These images show that the grid lines will stretch along the axis orthogonal to the lens axis, but will not affect the focus substantially along the axis parallel to the lens axis.

A example image of the flowfield inside the TAE tube is shown in Fig. 16, showing the measured density gradient field during operation of the rig. The optical spool piece was located just downstream of the regenerator. Hence, the helium gas has just been cooled by the regenerator, yielding density gradients in the gas. The image of the flow through the TAE appears to be slightly elliptical, which is caused by some of the light rays near the top and bottom of the glass tube being refracted outside of the glass tube. The light rays nearly tangent to the top and bottom of the tube get refracted into the glass and are totally internally reflected, yielding the clipping observed in the SAFS images (see the ray diagram of Fig. 15(a). The convective flow velocity computed using a sequential pair of SAFS images is plotted with velocity vectors in Fig. 16, where the color scale of the image ranges from 0 m/s to 4 m/s. The flow field within the TAE is observed to oscillate back and forth, but not in phase with the acoustic waves in the rig. This image and the associated velocity vectors show a time when the flow is reversing in the tube (to the left), and two counter-rotating

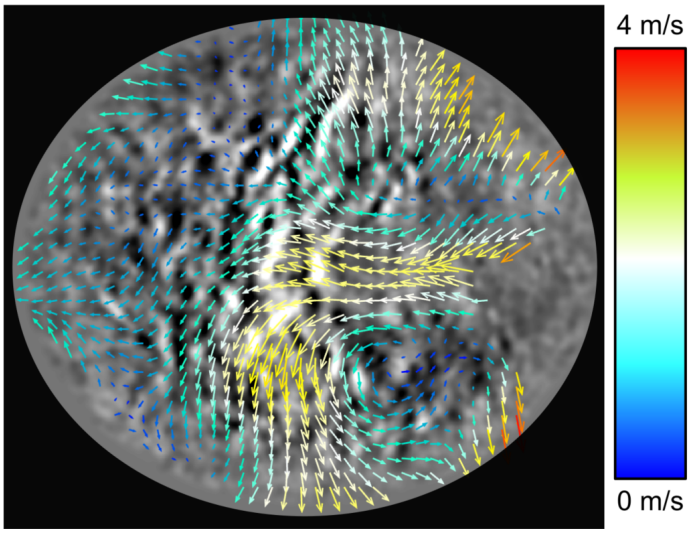

Fig. 16 Density gradient flowfield image inside the TAE spool piece, with convective velocity vectors plotted on the image, computed from two sequential SAFS images.

vortices are visible near the top-right and bottom-right of the image. The full image sequence clearly shows the evolving flow structure in the TAE tube, as well as the velocity vectors computed from this flow, demonstrating SAFS as a flow visualization tool in an extremely difficult environment.

VIII. Event-Based SAFS Imaging

Event-based cameras are a relatively recent advancement in camera technology [20] that provides an asynchronous stream of data, or events, that correspond to local changes in brightness on a per-pixel basis. An event generally provides a time-stamp, pixel index, and the sign of the brightness change. This strongly differs from conventional frame-based cameras that have been commonplace for decades and provides multi-bit data for all pixels over some integration time. In comparison, event-based cameras can provide data streams that help isolate intensity changes in time and space, and therefore lend themselves to a variety of scientific use cases.

Due to their recent development and relatively novel data stream, limited research exists on the processing and application of event-based data streams to fluid flows. Most research has been focused on it's application to particle-based methodologies, such as PTV and PIV [31–33]. Beyond PTV and PIV, there has been limited application to schlieren-based systems. Shiba *et al.* explored and developed a technique for the application of event-based cameras to background oriented schlieren [34]. Yet, to the authors knowledge, there exists no known use of event-based cameras with SAFS.

As an initial application of event-based cameras to SAFS, a similar system setup utilized for D-SAFS was used for event-based imaging. The μLCD was replaced with a RR with a line frequency of 2 lp/mm oriented horizontally. Next, the initial pulsed light source was replaced with a continuous LED light source (Lightspeed HPLS-36DD18B). Finally, the conventional camera was replaced with the event-based camera (iniVation DVXplorer). Both focusing and data capture was achieved by using a difluroethane jet (compressed gas duster) blowing through a 2.7 mm inner diameter needle. Event data was acquired utilizing the iniVation DV software with the effective framing rate set to 15000 eFPS and the sensitivity set to high. The jet was pulsed to provide a temporally evolving flow field.

Figure 17 illustrates the spatio-temporal nature of events and the isolation of the events as singular data points with varying polarity corresponding to either positive or negative changes in brightness. The asynchronous nature of event-based cameras can be difficult to interpret and to provide information in an intuitive manner as singular events provide little information [35]. One of the more intuitive interpretations is a frame-like accumulator that accumulates polarity at each pixel over some integration time. For the SAFS data acquired, multiple accumulator frames are shown in Fig. 18 with an integration time of 6.98 ms per frame. This shows the temporal evolution of the pulsed jet with a

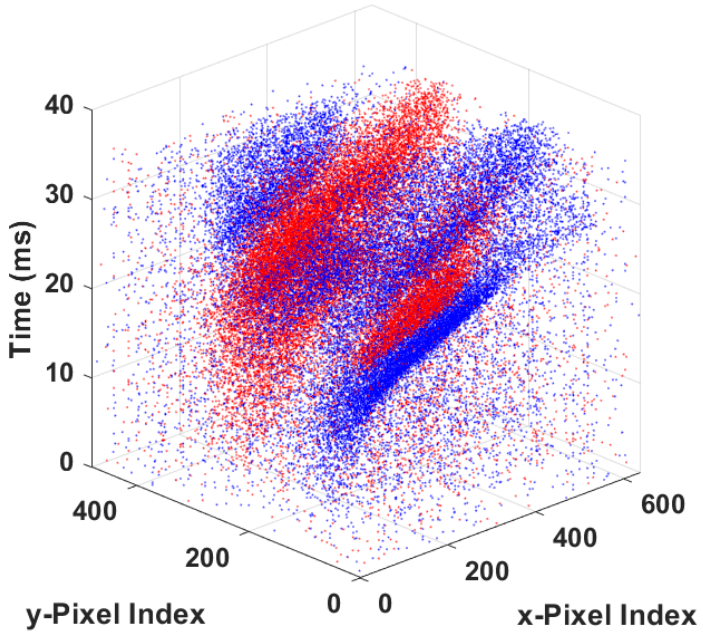

Fig. 17 Positive (red) and negative (blue) polarity events reported in space (x- and y-axis) and time as singular data points for a pulsed jet taken in a event-based SAFS system.

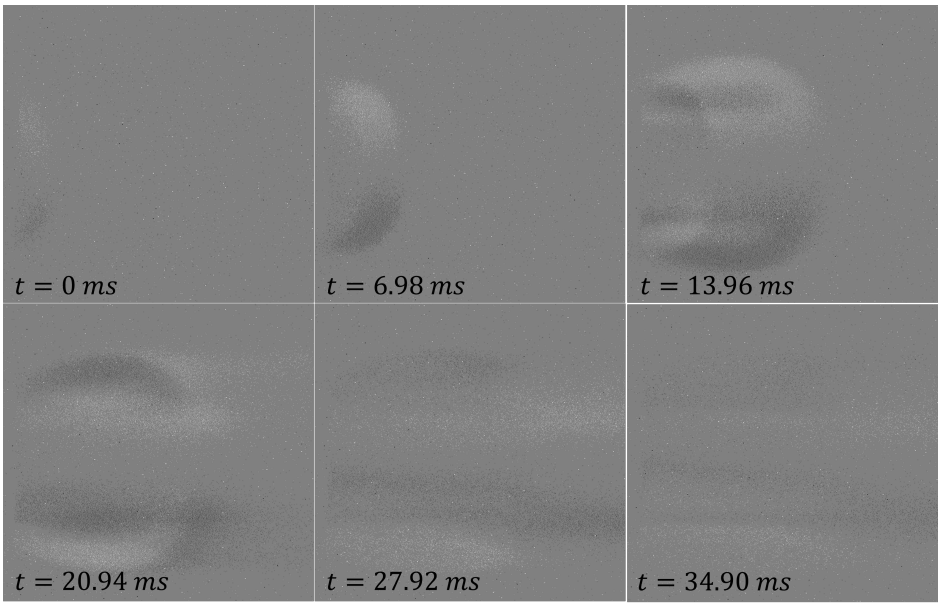

Fig. 18 Frame-like event accumulator for 6 different time steps with an integration time of 6.98 ms per frame for a pulsed jet in a SAFS system.

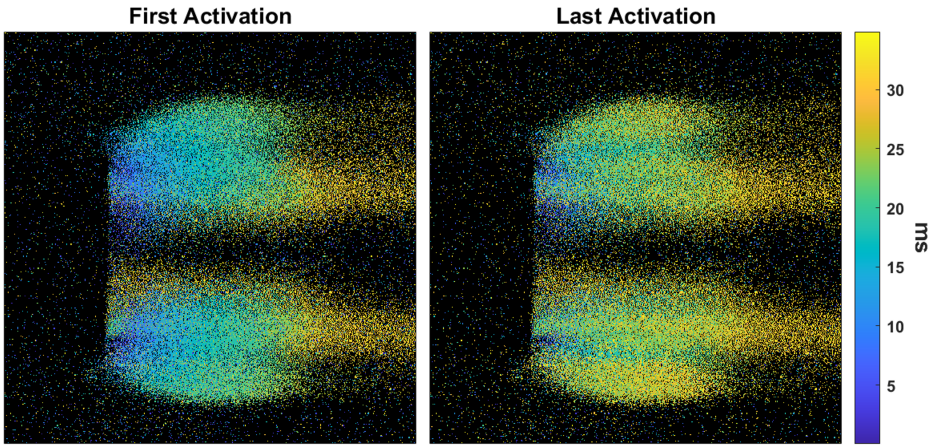

Fig. 19 Temporal coloring of the first (left) and last (right) activation of a pixel within a given time window of 0 to 34.90 ms for a pulsed jet in a SAFS system.

large activation of events in the first few frames subsequently followed by the reduction in the number of activation's as the laminar flow starts to setup with little temporal variation. The temporal information from the six frames in Fig. 18 can also be inferred using a "time surface" or temporal coloring where pixels can be colored based on the time of first or last activation. The temporal coloring is shown in Fig. 19 for both the first and last activation of each pixel. The first activation shows the propagation of the jet from left to right in time, where as the last activation shows the that pixels become inactive across a large portion of the image in a narrower time range. Additional exploration is needed on data processing methods to further extend the usefulness and applicability of an event-based SAFS, but the above representations show the richness of the supplied data.

IX. Spectral-Spatial Ronchi Rulings

The Ronchi ruling used in the SAFS system is typically a piece of glass with opaque chrome lines deposited on top in a high precision pattern (sometimes called chrome-on-glass). This type of *spatial filter* blocks light from passing through the optic at the opaque portions. Another type of filter, called a *spectral filter*, can be used to selectively attenuate or transmit different wavelengths of light, and come in various types including shortpass (allow short wavelengths to transmit), longpass (allow long wavelengths to transmit), notch (attenuate only a narrow wavelength range), or bandpass (transmit only a narrow wavelength range). Spectral filters are easily obtainable from a wide variety of vendors, and used in a wide range of optical devices and measurement techniques. They are typically manufactured in the normal round aperture or rectangular aperture form factor, for ease of inclusion in standard optical mounts. Various types of colors filters have found widespread use in schlieren measurements [1, 36]. One use of spectral filters is to obtain a simultaneous measurement of multiple directions of the density gradient field [37, 38], where a shortpass filter was used to obtain the vertical density gradients and a longpass filter to obtain the horizontal gradients.

For SAFS, using and/or stacking typical full-aperture spectral filters is not a viable method for creating the required Ronchi ruling pattern as the focus for each respective filter would be offset. Instead, these *spectral-spatial filters* must be manufactured as a single optic. Methods of creating these optics using, for example, ion-assisted electron-beam evaporative deposition (E-Beam IAD), advanced plasma deposition (APS), and atomic layer deposition (ALD) are cost-prohibitive, requiring an investment of thousands to tens of thousands of dollars to manufacture a single Ronchi ruling (based on the authors' discussions with optic manufacturing companies). Instead, these spectral spatial filters can be created using a film camera and color film (such as Kodak's E100 Ektachrome film), as shown in the schematic of Fig. 20. In this system, a 2D spectral spatial filter is created, by back-illuminating a Ronchi ruling (e.g., vertical grid lines) with blue light (RR^B) and another Ronchi ruling (e.g., horizontal grid lines) with red light (RR^R). Any number of spectral-spatial filter types can be created using this type of system. The simplest is a 1D Ronchi ruling of a single wavelength range. This 1D spectral-spatial filter can then be illuminated by a different wavelength of light without a

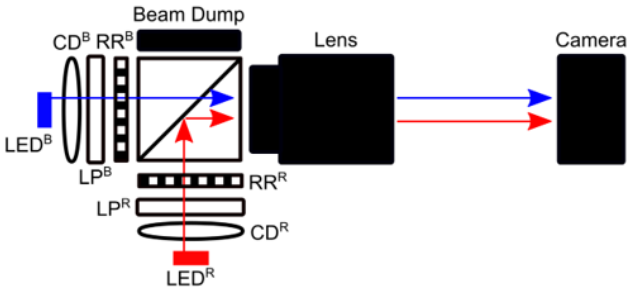

Fig. 20 Schematic of a setup used to create a 2D spectral-spatial Ronchi ruling, using blue and red LED light.

spatial filter, allowing for a simultaneous colinear non-SAFS measurements, such as PIV or photogrammetry. Finally, a 2D Ronchi ruling can be used to make simultaneous, unambiguous measurements of two directions of the density gradients.

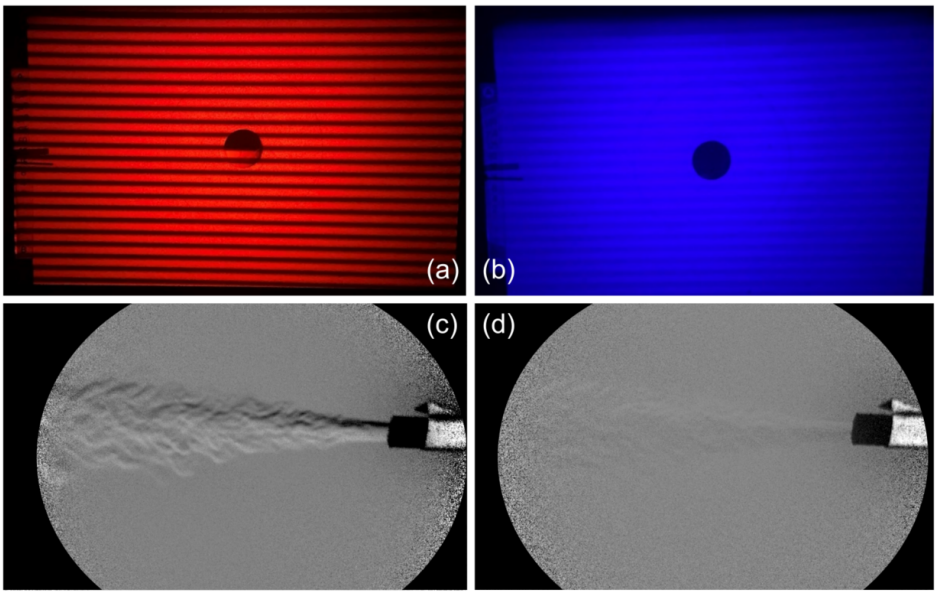

Fig. 21 (a,b) Images through the viewfinder of the Nikon film camera of the projected patterns from (a) red LED illumination with a Ronchi ruling and (b) blue illumination without a Ronchi ruling. (c,d) SAFS system images using the spectral-spatial filter using (c) red LED illumination and (d) blue LED illumination.

To create the 1D spectral-spatial filter, red light from an LED was used to back-illuminate a 1D Ronchi ruling as shown in Fig. 21(a), while blue light from an LED was used to fully illuminate the film, as shown in Fig. 21(b). These are images as seen through the viewfinder of the film camera, which is why the manual focus adjustment circle tool is visible at the center of the image. Both red and blue LEDs were included in the SAFS system setup with the 1D spectral-spatial filter at the normal Ronchi ruling position, and the flow from a canned air duster was used as the density object. Background-subtracted images of the flowfield are shown in Figs. 21(c) and 21(d) using red and blue LED illumination, respectively. The red light illumination of (c) returns the typical high quality schlieren imaging of the flow, while the blue light illumination of (d) shows nearly no flow signal, even with background subtraction and contrast enhancement. The small amount of flow signal visible in (d) is due to the non-ideal spectral separation of the blue channel of the film, as shown by the faint visible lines in (b). In both images (c) and (d), a small piece of retroreflective material is clearly visible on the nozzle tip, which can, for example, be used as a high contrast marker for simultaneous focusing schlieren and photogrammetry measurements. Testing of the 1D spectral-spatial filter for use with a colinear simultaneous focusing schlieren and PIV measurement also showed good results (not included in this paper).

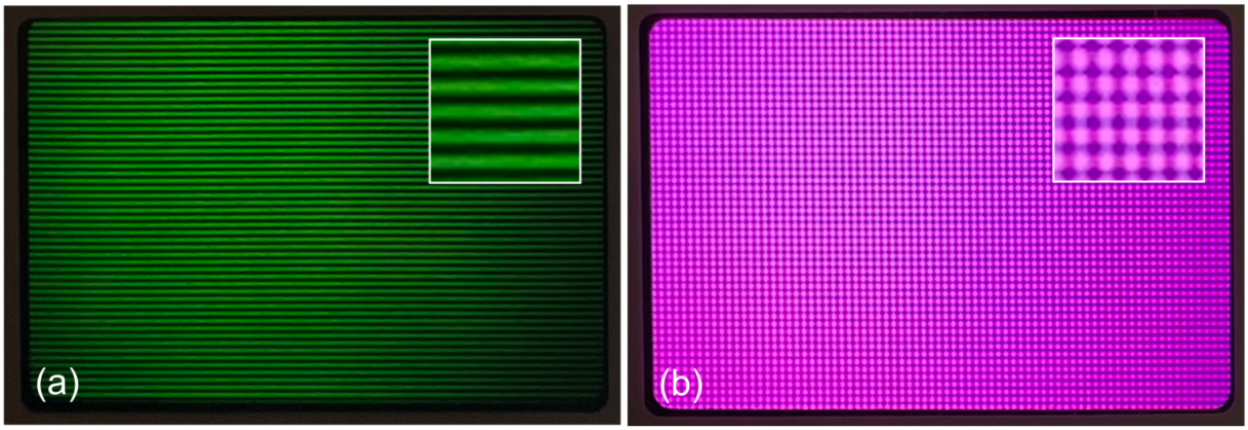

Fig. 22 (a) One-dimensional spectral-spatial filter using a horizontal grid illuminated with green light. (b) Two-dimensional spectral-spatial filter using a horizontal grid illuminated with red light and a vertical grid illuminated with blue light.

Another example of a 1D spectral-spatial filter is shown in Fig. 22(a), where a green LED was used to back-illuminate a Ronchi ruling onto the color film. As mentioned earlier, a 2D spectral-spatial filter with Ronchi ruling lines in both the horizontal and vertical directions can be manufactured, an example of which is shown in Fig. 22(b) using red and blue LED light for the back-illumination of the two orthogonally-aligned grids. By using a color camera for the image acquisition, the red and blue color channels each show either the vertical or horizontal density gradients. Note that a dichroic mirror and two monochrome cameras can also be used if higher spatial resolution is desired, or if high speed monochrome cameras are to be used.

This method of manufacturing of the spectral-spatial Ronchi rulings can also be used for spatial-only Ronchi rulings. In these instances, color film is not required, and black and white film can be used instead. The cost associated with the manufacturing can be kept below one dollar per Ronchi ruling, much cheaper than the hundreds of dollars for precision glass Ronchi rulings. Note, however, that there are several drawbacks associated with this method, such that it will not completely replace the need for precision glass Ronchi rulings, including the spatial resolution of the film, the size of the film, and the absence of an anti-reflection coating. This method of creation of a Ronchi ruling is the original method of creating cutoff grids for conventional focusing schlieren, but the method is slightly different because the imaging of the source grid on the catch side of the system must be performed at the cutoff grid plane, and after development of the cutoff grid film (and any resizing/magnification that needed to be performed), the focusing schlieren system could not be moved. For the spectral-spatial filters used here, the film is developed and mounted in 35 mm film holders to be inserted as the Ronchi ruling in the SAFS system.

X. Component Evaluation and Trade Studies

A. Ronchi Ruling Impact on Spatial Resolution

A method of determining the spatial resolution of an imaging system is through the use of the modulation transfer function (MTF), where the resolution is typically defined in units of linepairs per millimeter (lp/mm). A slant-edge target (e.g., Thorlabs R2L2S2P) can be used to obtain the MTF for both the horizontal and vertical directions of the imaging system. In a typical imaging system, the horizontal and vertical MTF curves should be very similar, but the addition of the Ronchi ruling grid in the SAFS system results in differences between the two, depending on the orientation of the grid lines.

The slant-edge target was placed at the focus plane of the SAFS system, and three configurations were tested, first with the Ronchi ruling vertically-oriented, second with the Ronchi ruling horizontally-oriented, and third without a Ronchi ruling present. Cropped view images of the corner of the slant edge target "L" are shown in Fig. 23a, with the Ronchi ruling orientation shown schematically on the image. Without the Ronchi ruling present, the left and top edges

of the dark region both appear sharp. However, with the Ronchi ruling either vertically or horizontally oriented, the left and top edges show signs of diffraction, respectively, which makes the edges appear blurred. From these images of the Ronchi ruling, the MTF was computed in both the vertical and horizontal directions of the images, and plotted in Fig. 23b. With the Ronchi ruling vertically oriented, the horizontal direction MTF (solid red) decreases to a lower value at a lower spatial resolution than the vertical direction MTF (solid black), as expected from the top left image of Fig. 23a. Conversely, with the Ronchi ruling horizontally oriented, the MTF curves swap, and the vertical direction MTF (dashed black) now has lower values at lower spatial resolutions than the horizontal direction MTF (dashed red). The solid black and dashed red lines correspond to the MTF for the vertical and horizontal direction from the image without the Ronchi ruling in the system. Note that these MTF curves in the direction orthogonal to the Ronchi ruling grid lines will change with different Ronchi ruling linepair spacing, and so the results presented here are only valid for this particular Ronchi ruling in this particular SAFS system. The spatial resolution of the SAFS system will need to be evaluated on a case-by-case basis, as it depends on all the optics and the camera used in the system.

B. Ronchi Ruling Line Pairs

The line spacing of the Ronchi ruling, measured in linepairs per millimeter (lp/mm), used for the source/cutoff grid has an impact on the quality of the resulting SAFS images, and for each system with its specific imaging distances, an ideal Ronchi ruling can be selected. To demonstrate this change in image quality, images were taken with a SAFS system to view a vertically-oriented helium jet, changing only the Ronchi ruling lp/mm (which was oriented with its lines vertical to be sensitive to horizontal density gradients). The SAFS images of the two jets with five different RRs with frequencies of 1, 2, 4, 10, and 15 lp/mm are shown in Fig. 24 for a qualitative comparison. The top row contains images of the full jet, while the bottom row shows a corresponding cropped region of the above image to show detail.

The ideal Ronchi ruling for this particular SAFS system, from the rulings that were available to test with, was a 2 lp/mm ruling. The image of the jet has high contrasting features, good resolution of the jet structures at various scales, and a sharp image of the jet nozzle. Decreasing to 1 lp/mm retains the sharp image of the jet nozzle and the good resolution of the jet structures, but the contrast of the jet structures is reduced. The lines from the 1 lp/mm Ronchi ruling are also faintly apparent in the image, but can be removed using FFT filtering as discussed in Sect. II.C. Increasing to 4 lp/mm, a high quality image of the entire jet is obtained, but the cropped view shows a slight smoothing of the jet structures. Part of this blurring is the onset of diffraction effects from the more closely-spaced Ronchi ruling grid lines. This can be seen at the right edge of the jet nozzle, where a slight double-image occurs in the horizontal direction, orthogonal to the orientation of the grid lines, as expected. At higher values of 10 lp/mm and 15 lp/mm, these effects

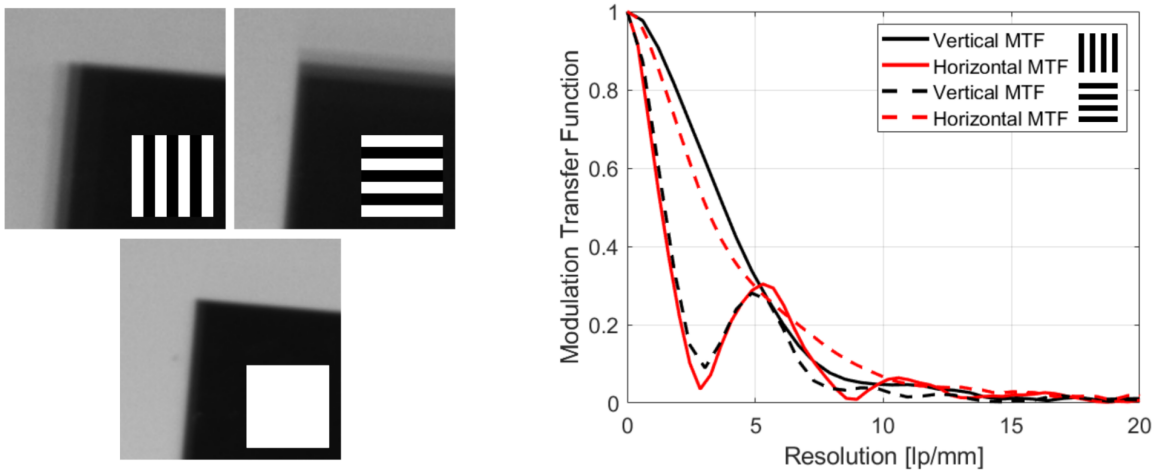

(a) (b)

Fig. 23 (a) Images of corner of slant edge target for vertical ruling, horizontal ruling, and no ruling. (b) MTF curves for vertical (black) and horizontal (red) directions, for vertical and horizontal orientations of the Ronchi ruling.

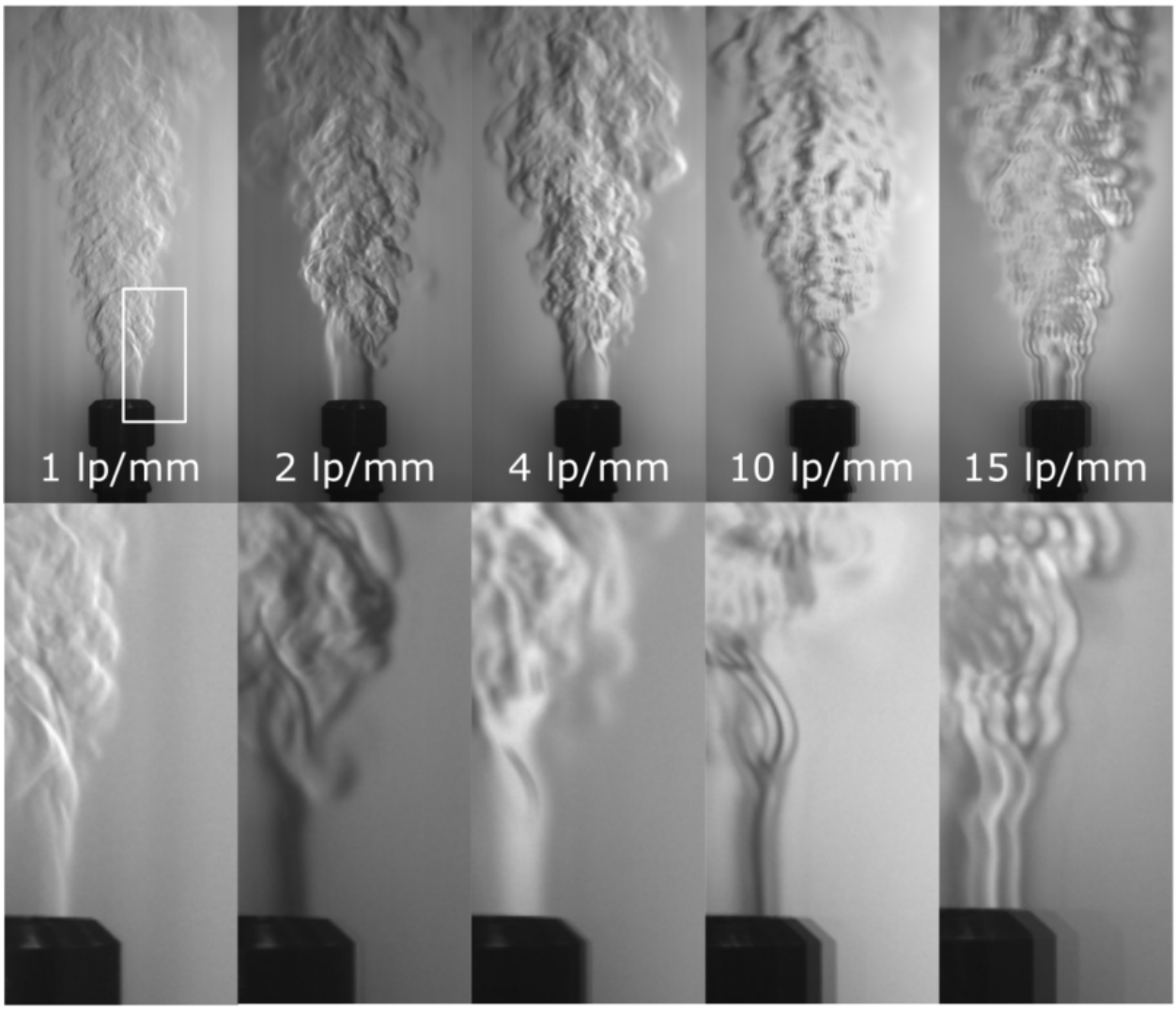

Fig. 24 SAFS images of a turbulent jet with varying Ronchi Rulings in place: 1 lp/mm, 2 lp/mm, 4 lp/mm, 10 lp/mm, and 15 lp/mm.

are more pronounced, with the jet appearing blurred and losing contrast, and the extent of diffraction clearly visible by the repeated images of the jet nozzle in the horizontal direction. The blurring and loss of contrast is at least partly due to the diffraction, where multiple copies of the flow structures are effectively averaged together at offset locations on the image sensor, smoothing out the high contrast, high resolution features seen in the 2 lp/mm image. Generally, lower lp/mm Ronchi rulings are used for smaller-scale systems, with smaller fields-of-view and imaging distances (e.g., NASA Langley 20-Inch Mach 6 and 31 Inch Mach 10, etc.), while higher lp/mm Ronchi rulings are used for larger-scale systems, with larger fields-of-view and imaging distances (e.g., NASA Langley National Transonic Facility, NASA Ames NFAC, etc.).

C. Rochon Prism Material Choice

Rochon prisms can be designed and manufactured with a variety of materials and splitting angles. Material choice is important as different materials and optical axis orientations may exhibit off-nominal behavior. Figure 25 presents a comparison of four Rochon prisms, with three designed with different materials (quartz/quartz (Q/Q), MgF_2/MgF_2, and glass/quartz (G/Q)) and a splitting angle of 7.5 arcmin and a fourth quartz/quartz with a splitting angle of 30

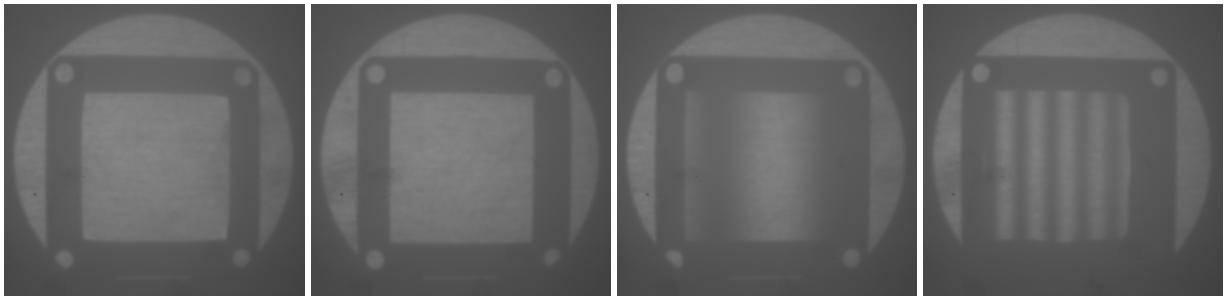

(a) (b) (c) (d)

Fig. 25 Collimated projection of light transmitted through four different Rochon prisms and a polarizer oriented to allow LVP light. From left to right, G/Q-7.5' (a), MgF_2/MgF_2-7.5' (b), (c) Q/Q-7.5' (c), and Q/Q-30') (d).

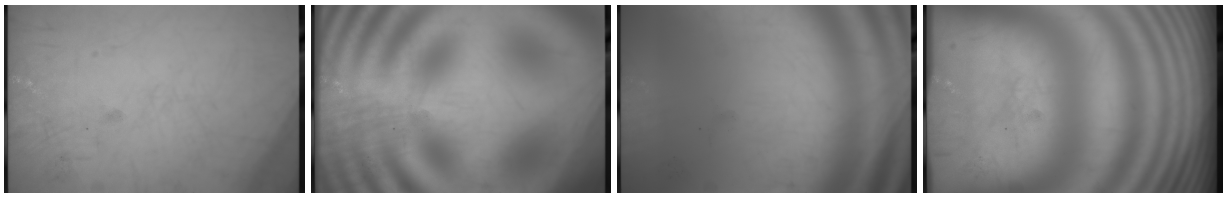

(a) (b) (c) (d)

Fig. 26 Projection of diverging light transmitted through four different Rochon prisms and a polarizer oriented to allow LVP light. From left to right, G/Q-7.5 arcmin (a), MgF_2/MgF_2-7.5 arcmin (b), (c) Q/Q-7.5 arcmin (c), and Q/Q-30 arcmin (d).

arcmin, illuminated with collimated, LVP light from an LED with a polarizer aft of the RP aligned to allow LVP light through. The dark regions in Fig. 25c and 25d are due to the optical activity inherent in Q/Q Rochon prisms as noted by Weisberger and Bathel [39] that rotates the polarization state within a portion of the Rochon prism. In contrast, both the G/Q and the MgF_2/MgF_2 prisms do not show any polarization rotation.

While collimated light is ideal, typical SAFS systems do not require the light to be collimated when passing through the RP. For comparison purposes, all four RP were placed in front of the collimating optic, where the light is still diverging, and the resulting projection was captured at the plane of the collimating optic. Figure 26 shows the resulting images that, when contrasted with Fig. 25, show a significant change in the behavior of the MgF_2/MgF_2 and QQ RPs with the occurrence of bright and dark radial-like bands.

The above measurements were all taken with a monochromatic light source, but if a white light source is used a similar effect can be observed with a chromatic variation rather than light and dark fringes. Figure 27 shows images of loosely collimated white light passed through the RPs with varying levels of incidence that demonstrate the chromatic variation in all RPs except for the G/Q-7.5 arcmin prism. The incidence was varied in a rough manner to demonstrate the appearance and disappearance of the chromatic fringes for the various RPs. This rotation was performed from a large counter-clockwise rotation to a similarly large clockwise rotation of the prisms. It should be noted that the presented behavior is similar for light incident on either face of the RP with the chromatic variations flipping about the vertical axis.

Figure 25, Fig. 26, and Fig. 27 demonstrate that the polarization output varies over the clear aperture for both RP designed with a configuration of MgF_2/MgF_2 and Q/Q. The G/Q prism was the only RP tested that didn't exhibit any polarization variation with either collimated or diverging light. While polarization variation in the RP is generally considered non-ideal for SAFS-based systems, Weisberger *et al.* [22] found significant improvements in quality of SAFS images when utilizing the 30 arcmin quartz/quartz RP when windows in the 0.3-M Transonic Cryogenic Tunnel at NASA Langley Research Center exhibited significant birefringence largely attributed to the mechanical stresses and temperature gradients in the window at cryogenic temperatures.

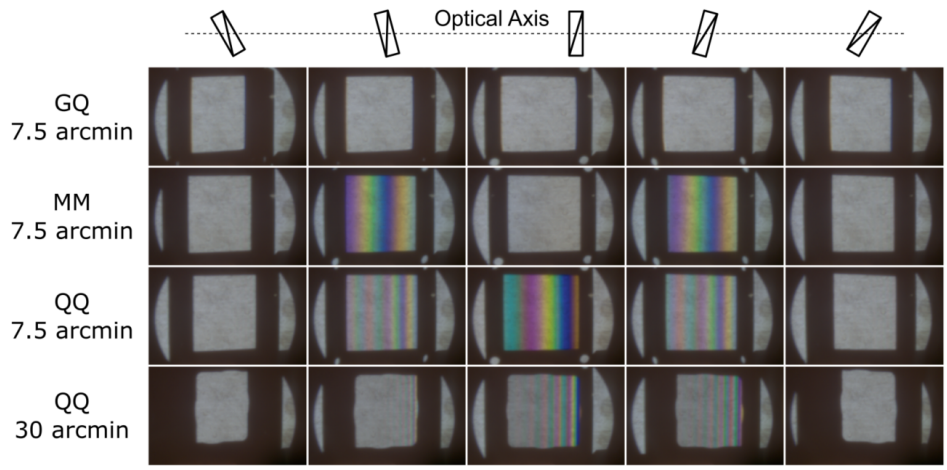

Fig. 27 Loosely collimated and linearly polarized light transmitted through the front face of four different Rochon prims (From top to bottom, G/Q-7.5 arcmin, MgF_2/MgF_2-7.5 arcmin, Q/Q-7.5 arcmin, and Q/Q-30 arcmin.) with varying rotations (counter-clockwise to clockwise from left to right, respectively).

D. Rochon Prism Sensitivity Adjustment

The Rochon prism is used in the SAFS system to adjust the sensitivity, effectively acting as a knife-edge insertion adjustment in a conventional schlieren system. In a conventional focusing schlieren system, this adjustment is achieved by translating the cutoff grid in a direction orthogonal to the axis of the grid lines and the optical axis, since the source grid and cutoff grid are separate optics. In the SAFS system, this cannot be done because the source and cutoff grids are the same optic (i.e., the Ronchi ruling). Instead, the Rochon prism is used to refract the incoming light slightly, depending on the splitting angle of the prism (dictated by the materials used in its construction and the structure angle of the two halves of the prism). Because the incoming beam is refracted at a fixed angle from the optical axis, adjustment of the sensitivity must be achieved by moving the Rochon prism relative to the Ronchi ruling.

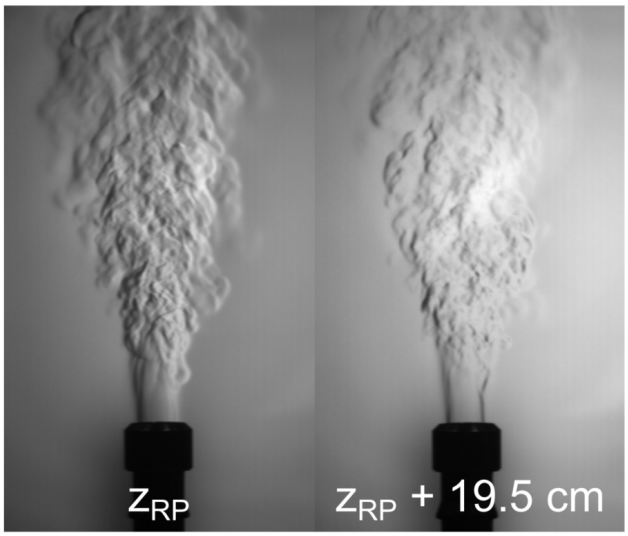

Fig. 28 SAFS images of a helium jet demonstrating sensitivity adjustment by translation of the Rochon prism along the axis over 19.5 cm.

The method of sensitivity adjustment discussed in detail in Section 3.4 of Weisberger and Bathel [17] is to translate the prism along the optical axis. Depending on the SAFS system, this prism translation can achieve a full period of

sensitivity adjustment, from bright-field (no cutoff) to dark-field (full cutoff), and anywhere in between. However, as shown in Fig. 28 for a different SAFS system, even the large translation of 19.5 cm was not sufficient to change the sensitivity from near 50% cutoff to bright-field. Note that in Ref. [17], the Rochon prism was located between the Ronchi ruling and the field lens, but for the SAFS system used to obtain the images in Fig. 28, the Rochon prism was located after the field lens due to insufficient space between the Ronchi ruling and the field lens (which is typical of larger imaging distance systems). Because the split light exiting the Rochon prism is then imaged through the field lens before being incident on the Ronchi ruling, the prism translation may have a smaller impact on the sensitivity adjustment than if the prism were located between the Ronchi ruling and field lens.

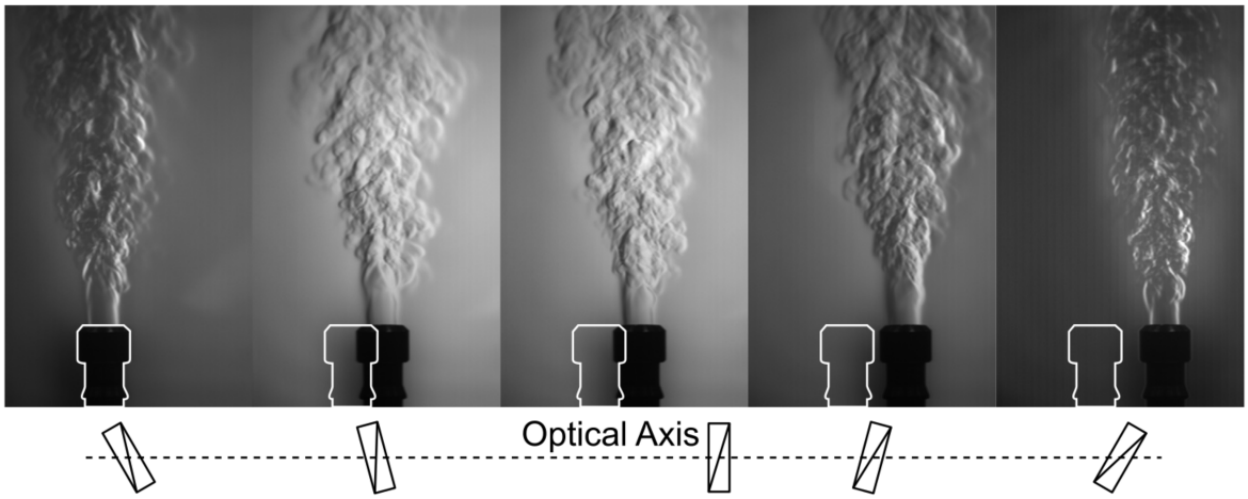

Fig. 29 SAFS images of helium jet demonstrating sensitivity adjustment by rotation of the Rochon prism. The white outline of the jet from the left-most image is repeated across all images to show shift of jet nozzle, and the rotation of the Rochon prism relative to the optical axis of the SAFS system is shown at the bottom.

Translation of the prism over long distances to achieve the necessary sensitivity adjustment is not always feasible, and purchasing new prisms with a different splitting angles can be cost-prohibitive. A simple method of sensitivity adjustment in spatially constrained environments is to rotate the prism about an axis orthogonal to the splitting plane. Results from the same SAFS system used for the translation measurement, this time using a prism rotation for the sensitivity adjustment, can be seen in the images of Fig. 29. A top-down schematic of the rotation of the prism about the optical axis (Ronchi ruling grids lines are vertical, out of the page) is shown at the bottom of the figure for each image, where the middle image is for the nominal no-rotation position of the prism. When the prism is rotated either clockwise or counter-clockwise, the sensitivity adjustment is visible, demonstrating the viability of this space-constrained method of adjustment. Note, however, that the position of the image of the object also shifts in the image when the prism is rotated. The jet nozzle position in the left-most image is repeated in the other images to show this translation in the image. As long as the flow of interest remains in the field-of-view of the SAFS images, this rotation of the prism can be used. An example of this space-constrained Rochon prism rotation for sensitivity adjustment is shown in Section VI.

E. Quarter-Wave Plate vs. Quarter-Wave Film

The quarter-wave retarder is used to convert the outgoing linear polarization state to circular polarization such that the RBG can reverse the handedness of the circular polarization, and reverse passage through the quarter-wave retarder can result in an effective 90° rotation of the linear polarization state. The quarter-wave retarder must be located after the Rochon prism, but aside from this stipulation, it can be located anywhere between the Rochon prism and the RBG. The location of the quarter-wave retarder is typically dictated by the limitations of the facility where the testing is taking place. For example, if the testing does not require the flow to be separated from the SAFS system with a window, the quarter-wave retarder can be placed directly next to the RP without any degradation to the image performance. However, if a window is placed between the SAFS system and the flow, it is beneficial to move the quarter-wave retarder after the window(s), such that it is directly in front of the RBG, reducing/eliminating any unwanted window reflections visible in

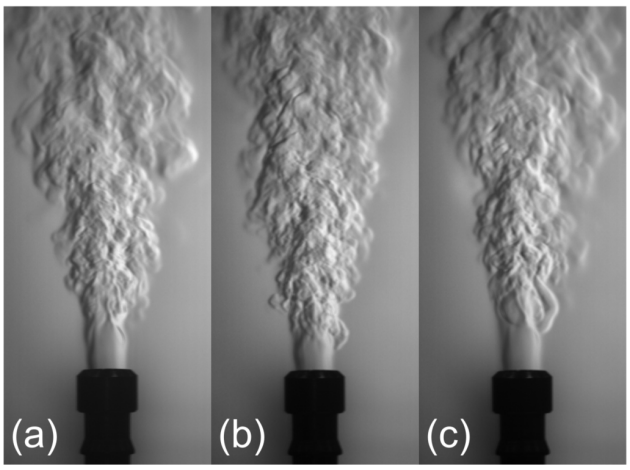

Fig. 30 SAFS images with (a) the QWP after the RP, (b) the QWF after the RP, and (c) the QWF on the RBG.

the images.

Given these differences in the quarter-wave retarder position, two options are available: a quarter-wave plate (QWP) and a quarter-wave film (QWF). Example images using these two options in different positions are shown in Fig. 30. In Fig. 30(a), the QWP is placed directly after the RP. In Fig. 30(b), the QWP was replaced with a QWF, still placed directly after the RP. Finally, in Fig. 30(c) the QWF was moved to a position directly in front of the RBG. In all three images, the jet flow is well-resolved and the contrast is good, with very little difference visible between all three.

Whether to choose a QWP or a QWF depends on the application and situational limitations. In general, QWPs are manufactured with tight tolerances, are more expensive, and are rigid, while QWF can be quite inexpensive, but is a very thin plastic film that can be easily damaged when handled repeatedly. QWPs are limited to smaller apertures (generally 50.8 mm maximum), whereas QWF can be purchased in large sheets (e.g., 300 mm-square sheets), which can then be cut down to an appropriate size. If using the QWF adjacent to the RP, then one sheet can be used for many instances of the system. The QWP can be easily mounted in a rotation mount for precise rotation to maximize the signal, while the QWF is typically fixed to a surface using tape, and fine adjustment of the rotation of the film is not feasible. In testing performed at the NASA LaRC Transonic Dynamics Tunnel (TDT), the QWF was placed in the plenum, a cavity between two sets of windows. Because there are slots in the tunnel wall, moving currents in the plenum caused the QWF to wave a little, even after all four sides were taped in place. Finally, the QWF can only be placed adjacent the RBG to eliminate window reflections if the RBG is located outside the wind tunnel, otherwise the film may rip and become dislodged from the wall. For example, in testing at the 0.3-M TCT and the NTF, as discussed in detail in Ref. [22], the RBG was adhered to the wall inside the tunnel test section, and so a QWP was used, placed adjacent to the RP.

XI. Conclusions

A broad range of recent applications and development of self-aligned focsing schlieren-based systems is presented in the current manuscript. This includes the development of digital, Scheimpflug, and plenoptic SAFS imaging and further extension of SAFS to use event-based cameras. SAFS was also applied to difficult and constrained facilities. Furthermore, various important components are characterized via simple trade studies that demonstrate both behavior and usability of the respective component.

Digital SAFS (D-SAFS) performance was demonstrated and shown to exhibit repeated image artifacts from diffraction of light through the pixels and strong background that masks out the underlying schlieren signal. The polarization control was shown to be highly dependent on wavelength and that current experiments have utilized wavelengths that are off-nominal. Future work is needed to further characterize D-SAFS with different wavelengths of light used as the input source and to help eliminate the influence of the diffraction artifacts evident in acquired images.

Scheimpflug and plenoptic SAFS imaging were demonstrated and shown to extend the capabilities of SAFS to extended fields-of-view and refocus images post data acquisition, respectively. Further progress was shown on the

generation and replacement of Ronchi rulings with spectral-spatial filters that enable the simultaneous capture of horizontal and vertical gradients. The method of manufacturing the filters was shown to have a relatively low cost when compared to the acquisition of high-quality glass Ronchi rulings that are typical used in SAFS. Finally, event-based cameras were utilized and demonstrated in a SAFS-based system to provide a spatio-temporal data stream of SAFS events. Further work looks to explore various data processing techniques and events-based representations to better utilize the unique data streams and provide useful, intuitive measurements.

SAFS was demonstrated to be a relatively robust technique with a broad range of usability in various challenging environments and facilities. A large-scale SAFS system was designed and applied in the largest wind tunnel facility in the world, the National Full-Scale Aerodynamics Complex (NFAC) 80- by 120-Foot Wind Tunnel at NASA Ames Research Center. Additionally, a typical SAFS system was utilized to image through curved windows in the Thermal Acoustic Engines (TAE) rig at NASA Glenn Research Center. It was shown to be capable of capturing the density gradients within the facility with enough quality to obtain SAFS-based convective velocity measurements.

Finally, the current work presented evaluations and trade studies of Ronchi rulings (RR), Rochon prisms (RP), and the use of quarter-wave film (QWF) versus quarter-wave plates (QWP). The line spacing in Ronchi rulings was shown to have a strong effect on the spatial resolution of the system and the sensitivity of the SAFS images. All of these factors need to be evaluated and adjusted on a case-by-case basis, as they are highly dependent on the entire optical setup utilized. Various RPs were shown to exhibit off-nominal polarization variation across their clear aperture. Although, this was highly dependent on the materials used with only the glass/quartz RP displaying no off-nominal behavior. Furthermore, translation and rotation of the RP were shown to have relatively large impacts on the sensitivity of the SAFS measurements made. Finally, QWF was shown to be relatively interchangeable with QWP although this depends on the application and situational limitations.

Acknowledgments

This work was supported by the NASA Plume Surface Interaction (PSI) project, Transformation Tools and Technologies (TTT) project, Hypersonic Technologies Project (HTP), and the Aerosciences Evaluation and Test Capabilities (AETC) project. The authors wish to thank Mr. Stephen B. Jones and Mr. W. Holt Ripley for their assistance with the various experimental setups. The authors would like to acknowledge Robert Ren of United Crystals for assistance with the fabrication of all Rochon prisms used in this work, Mr. David Shindell of Data Optics, Inc. for his assistance with fabrication of the chrome-on-glass Ronchi rulings used in this work, Mr. Joshua Carter of Dwayne's Photo for assistance with processing of the spectral-spatial Ronchi rulings, and Mr. Robin Brugger and Mr. Edmund Schaller of BBS Bild und Lichtsysteme GmbH for their assistance with the D-SAFS μLCD units. The use of trademarks or names of manufacturers in this report is for accurate reporting and does not constitute an official endorsement, either expressed or implied, of such products or manufacturers by the National Aeronautics and Space Administration.

Technology Transfer Statement

Several of the technologies described in this document may be protected by U.S. patents and patent applications, such as U.S. Patent Nos. 11,650,151, 12,072,286, and others. More information about these technologies, including how to license the patents, can be found at `https://technology.nasa.gov` (LAR-TOPS-348 and LAR-TOPS-349).

References

[1] Settles, G., *Schlieren and Shadowgraph Techniques: Visualizing Phenomena in Transparent Media*, Springer Berlin Heidelberg, 2001. https://doi.org/10.1007/978-3-642-56640-0.

[2] Gladstone, J., and Dale, T., "XIV. Researches on the refraction, dispersion, and sensitiveness of liquids," *Philosophical Transactions of the Royal Society of London*, Vol. 153, 1863, pp. 317–343. https://doi.org/10.1098/rstl.1863.0014.

[3] Toepler, A. J. I., *Beobachtungen nach einer neuen optischen methode: Ein beitrag experimentalphysik*, 157, W. Engelmann, 1906.

[4] Raffel, M., Richard, H., and Meier, G. E. A., "On the applicability of background oriented optical tomography for large scale aerodynamic investigations," *Experiments in Fluids*, Vol. 28, No. 5, 2000, pp. 477–481. https://doi.org/10.1007/s003480050408, URL https://doi.org/10.1007/s003480050408.

[5] Raffel, M., Tung, C., Richard, H., Yu, Y., and Meier, G. E. A., "Background oriented stereoscopic schlieren (BOSS) for full-scale helicopter vortex characterization," *9th International Symposium on Flow Visualization*, Heriot-Watt University, Edinburgh, 2000.

[6] Richard, H., and Raffel, M., "Principle and applications of the background oriented schlieren (BOS) method," *Measurement Science and Technology*, Vol. 12, No. 9, 2001, p. 1576. https://doi.org/10.1088/0957-0233/12/9/325, URL https://dx.doi.org/10.1088/0957-0233/12/9/325.

[7] Raffel, M., "Background-oriented schlieren (BOS) techniques," *Experiments in Fluids*, Vol. 56, No. 3, 2015, p. 60. https://doi.org/10.1007/s00348-015-1927-5, URL https://doi.org/10.1007/s00348-015-1927-5.

[8] Hartmann, J., "The Acoustic Air-Jet Generator," Technical Translation (2021) NASA-TT-20210016495, Technical University of Denmark, Nov. 1940.

[9] Schardin, H., "Schlieren methods and their applications," NASA-TT-F12731 (1970), 1942.

[10] Burton, R. A., "A modified Schlieren apparatus for large areas of field." *Jounral of the Otpical Scoiety of America*, Vol. 39, No. 11, 1949, p. 907.

[11] Weinstein, L. M., "Large-field high-brightness focusing schlieren system," *AIAA Journal*, Vol. 31, No. 7, 1993, pp. 1250–1255. https://doi.org/10.2514/3.11760.

[12] Buckner, B., Trolinger, J., and L'esperance, D., "Digital focusing schlieren imaging," 2015. https://doi.org/10.1117/12.2189533.

[13] Schoegl, I., Pisano, A., and Sedky, G., "Development of a Compact Focusing Color Schlieren Technique," 2016. https://doi.org/10.2514/6.2016-1765.

[14] L'Esperance, D., and Buckner, B. D., "Focusing schlieren systems using digitally projected grids," *Applied Optical Metrology II*, Vol. 10373, edited by E. Novak and J. D. Trolinger, International Society for Optics and Photonics, SPIE, 2017, p. 103730R. https://doi.org/10.1117/12.2274079, URL https://doi.org/10.1117/12.2274079.

[15] Buckner, B. D., and L'Esperance, D., "Schlieren unwrapped: distortion correction in digital focusing schlieren," *Applied Optical Metrology III*, Vol. 11102, edited by E. Novak and J. D. Trolinger, International Society for Optics and Photonics, SPIE, 2019, p. 111020R. https://doi.org/10.1117/12.2528081, URL https://doi.org/10.1117/12.2528081.

[16] Bathel, B. F., and Weisberger, J. M., "Compact, self-aligned focusing schlieren system," *Opt. Lett.*, Vol. 46, No. 14, 2021, pp. 3328–3331. https://doi.org/10.1364/OL.428011, URL https://opg.optica.org/ol/abstract.cfm?URI=ol-46-14-3328.

[17] Weisberger, J. M., and Bathel, B. F., "Single source/cutoff grid, self-aligned focusing schlieren system," *Experiments in Fluids*, Vol. 63, No. 1, 2022, p. 38. https://doi.org/10.1007/s00348-022-03389-7, URL https://doi.org/10.1007/s00348-022-03389-7.

[18] Bathel, B. F., Weisberger, J. M., Page, W. E., Lalonde, E. J., and Jones, S. B., "Digital self-aligned focusing schlieren," *Opt. Lett.*, Vol. 49, No. 4, 2024, pp. 778–781. https://doi.org/10.1364/OL.511274.

[19] Bathel, B. F., Boyda, M. T., and Weisberger, J. M., "Self-aligned focusing schlieren in optically constrained environments," *Applied Optics*, Vol. 63, No. 26, 2024, p. 6831. https://doi.org/10.1364/ao.533087.

[20] Lichtsteiner, P., Posch, C., and Delbruck, T., "A 128× 128 120 dB 15 μs Latency Asynchronous Temporal Contrast Vision Sensor," *IEEE Journal of Solid-State Circuits*, Vol. 43, No. 2, 2008, pp. 566–576. https://doi.org/10.1109/JSSC.2007.914337.

[21] Weisberger, J. M., and Bathel, B. F., "Colinear focused laser differential interferometry and self-aligned focusing schlieren," *Applied Optics*, Vol. 62, No. 18, 2023, p. 4958. https://doi.org/10.1364/ao.489897.

[22] Weisberger, J. M., Bathel, B. F., Danehy, P. M., Boyda, M. T., Tyrrell, O. K., Ripley, W. H., Jones, G. S., Burns, R. A., Kwok, A. K., and Jones, S. B., "Self-Aligned Focusing Schlieren at the 0.3-M Transonic Cryogenic Tunnel and the National Transonic Facility," *AIAA SciTech 2024 Forum*, American Institute of Aeronautics and Astronautics, 2024. https://doi.org/10.2514/6.2024-2500.

[23] Scheimpflug, T., "Method of Distorting Plane Images by Means of Lenses and Mirrors," , Feb. 1904. U.S. Patent.

[24] Adelson, E. H., and Wang, J. Y. A., "Single Lens Stereo with a Plenoptic Camera," *IEEE Transactions on Pattern Analysis and Machine Intelligence*, Vol. 14, No. 2, 1992, pp. 99–106. https://doi.org/10.1109/34.121783.

[25] Davis, J. K., Clifford, C. J., Kelly, D. L., and Thurow, B. S., "Tomographic background oriented schlieren using plenoptic cameras," *Measurement Science and Technology*, Vol. 33, No. 2, 2021, p. 025203. https://doi.org/10.1088/1361-6501/ac3b09.

[26] Hall, E., Davis, J., Guildenbecher, D., and Thurow, B., *Plenoptic Background Oriented Schlieren Imaging*, Springer International Publishing, 2024, pp. 357–367. https://doi.org/10.1007/978-3-031-39062-3_19.

[27] Kerth, P., Hermann, T. A., and McGilvray, M., "Three-Dimensional Focusing Schlieren using a Plenoptic Camera," *International Conference on Flight Vehicles, Aerothermodynamics and Re-entry Missions and Engineering*, 2019. https://doi.org/10.5287/bodleian:5RErGzjj0.

[28] Norman, T., Schaeffler, N., Overmeyer, A., Heineck, J., Chairer, E., Wagner, L., Yamauchi, G., Dominguez, M., Sheikman, A., Ramasamy, M., and Cameron, C., "Fundamental Test of a Hovering Rotor: Comprehensive Measurements for CFD Validation," *Proceedings of the Vertical Flight Society 79th Annual Forum*, The Vertical Flight Society, 2023, pp. 1–27. https://doi.org/10.4050/f-0079-2023-17983.

[29] Ramasamy, M., Heineck, J., Yamauchi, C., Schairer, E., and Norman, T., "Comprehensive Aerodynamic Analysis of PIV Measurements in the NFAC 80- by 120-ft Test Section Towards Understanding HVAB Hovering Rotor Characteristics," *Proceedings of the Vertical Flight Society 80th Annual Forum*, The Vertical Flight Society, 2024, pp. 1–30. https://doi.org/10.4050/f-0080-2024-1351.

[30] Rodriguez, L. A., Dyson, R., Wernet, M., and Leibach, R., "Thermoacoustic Thermal Management for Electric Aircraft," *to be presented at AIAA SciTech 2025 Forum*, American Institute of Aeronautics and Astronautics, 2025.

[31] Drazen, D., Lichtsteiner, P., Häfliger, P., Delbrück, T., and Jensen, A., "Toward real-time particle tracking using an event-based dynamic vision sensor," *Experiments in Fluids*, Vol. 51, No. 5, 2011, pp. 1465–1469. https://doi.org/10.1007/s00348-011-1207-y, URL https://doi.org/10.1007/s00348-011-1207-y.

[32] NI, Z., PACORET, C., BENOSMAN, R., IENG, S., and RÉGNIER*, S., "Asynchronous event-based high speed vision for microparticle tracking," *Journal of Microscopy*, Vol. 245, No. 3, 2012, pp. 236–244. https://doi.org/https://doi.org/10.1111/j.1365-2818.2011.03565.x, URL https://onlinelibrary.wiley.com/doi/abs/10.1111/j.1365-2818.2011.03565.x.

[33] Willert, C. E., and Klinner, J., "Event-based imaging velocimetry: an assessment of event-based cameras for the measurement of fluid flows," *Experiments in Fluids*, Vol. 63, No. 6, 2022, p. 101. https://doi.org/10.1007/s00348-022-03441-6, URL https://doi.org/10.1007/s00348-022-03441-6.

[34] Shiba, S., Hamann, F., Aoki, Y., and Gallego, G., "Event-Based Background-Oriented Schlieren," *IEEE Transactions on Pattern Analysis and Machine Intelligence*, Vol. 46, No. 4, 2024, pp. 2011–2026. https://doi.org/10.1109/TPAMI.2023.3328188.

[35] Gallego, G., Delbrück, T., Orchard, G., Bartolozzi, C., Taba, B., Censi, A., Leutenegger, S., Davison, A. J., Conradt, J., Daniilidis, K., and Scaramuzza, D., "Event-Based Vision: A Survey," *IEEE Transactions on Pattern Analysis and Machine Intelligence*, Vol. 44, No. 1, 2022, pp. 154–180. https://doi.org/10.1109/TPAMI.2020.3008413.

[36] Settles, G. S., "Color Schlieren Optics - A Review of Techniques and Applications," *Proceedings of the International Symposium on Flow Visualization*, 1980.

[37] Martinez-Gonzalez, A., and Hernandez, D. M., "Horizontally and vertically sensitive schlieren and shadowgraph system," *Optics Letters*, Vol. 47, No. 14, 2022, p. 3596. https://doi.org/10.1364/ol.467453.

[38] Martínez-González, A., Moreno-Hernández, D., León-Rodríguez, M., Carrillo-Delgado, C., and Cossío-Vargas, E., "Simultaneous Schlieren-Shadowgraph Visualization and Temperature Measurement Fields of Fluid Flow Using One Color CCD Camera," *Sensors*, Vol. 22, No. 23, 2022, p. 9529. https://doi.org/10.3390/s22239529.

[39] Weisberger, J. M., and Bathel, B. F., "Characterization of Rochon Prisms for Bi-Directional Imaging Applications," Technical Memorandum NASA-TM-20210026232, NASA Langley Research Center, Jan. 2022.